Available online at www.sciencedirect.com
SCIENCE DIRECT®
Tectonophysics 374 (2003) 135–161
TECTONOPHYSICS
www.elsevier.com/locate/tecto

Shear wave splitting beneath South Kamchatka during the 3-year period associated with the 1997 Kronotsky Earthquake

Margarita N. Luneva[a,1], Jung Mo Lee[b,*]

[a] *Institute of Tectonics and Geophysics, Far East Branch of the Russian Academy of Sciences, 65 Kim-Yu-Chen Street, 680000 Khabarovsk, Russia*
[b] *Department of Geology, Kyungpook National University, Taegu 702-701, South Korea*

Received 26 April 2002; accepted 4 August 2003

Abstract

Shear wave splitting measurements in South Kamchatka during the 3-year period (1996–1998) in which the Kronotsky Earthquake ($M=7.7$, December 5, 1997) occurred are used to determine anisotropic parameters of the subduction zone and shear wave splitting variations with time. The local small seismic events recorded at the Petropavlovskaya IRIS station (PET) were analyzed. The dominant azimuths of the fast shear wave polarizations for the 3-year period are defined within N95 ± 15°E, which are consistent with the general Pacific Plate motion direction. Modeling of fast shear wave polarizations shows that HTI model with the symmetry axis oriented along N15°E ± 10° fit well the observed data for events the focal depths of which are less than 80 km. For the greater depths, the orthorhombic symmetry of medium is not excluded. The anisotropy coefficient increases generally with depth from 1–2% in the crust to 4–7.5% in the subducting plate. Variations in time delays show a general increase up to 10–15 ms/km during 1996–1997 before the large crustal earthquake series ($M \approx 5.5$–7) in the Avacha Bay and before the Kronotsky Earthquake. Analysis of fast S-wave azimuths of mantle events reveals a temporal cyclic variation. The most regular variations are observed for fast azimuths of deep events with a period of about 172 days over the 3-year period. The fast polarizations of crustal events behave comparatively stable. It is assumed that the major instabilities in stress state are localized in the descending slab and influenced the upper mantle and comparatively stable crust.

Keywords: Anisotropy; Shear wave splitting; Kamchatka

1. Introduction

The Kamchatka region belongs to the Kuril–Kamchatka seismically active subduction zone. The Pacific Plate subducts westward beneath the Kamchatka with a dip angle of about 55° and a rate of about 8 cm/year. The maximum depths of the downgoing slab reach about 500 km in the southern part of Kamchatka and shallow gradually towards the north (e.g., Gorbatov et al., 1999). Analysis of seismic activity in the Kamchatka area during the last decade reveals temporal changes in the seismicity level and localization of seismically active and silent zones, which indicate the developing of mechanical and stress instabilities

* Corresponding author. Tel.: +82-53-950-5354; fax: +82-53-950-5362.
E-mail addresses: margo@itig.as.khb.ru (M.N. Luneva), jung@knu.ac.kr (J.M. Lee).
[1] Tel.: +7-4212-227189; fax: +7-4212-227684.

0040-1951/$ - see front matter © 2003 Elsevier B.V. All rights reserved.
doi:10.1016/j.tecto.2003.08.002

in heterogeneous medium (Sobolev, 1999, 2001). Based on the regional catalogue compiled by the Kamchatka Experimental Methodical Seismological Department of Geophysical Services of the Russian Academy of Sciences (KEMSD GS RAS), the maximum level of the regional seismicity refers to the period of 1996–1998, when annual amount of earthquakes jumps up to 3985–5726 comparing with 1100–1440 for the previous years. On December 5, 1997 the strong shallow earthquake of $M=7.7$ occurred in the Kronotsky Bay at the eastern Kamchatka offshore. It is considered as the strongest earthquake over the last 25 years. The main shock rupture is defined as a reverse fault striking S40 $\pm$ 22°W and propagating with a speed of 4 km/s (Gusev and Pavlov, 1998). The direction of compressive tectonic stress estimated is consistent with a general motion direction of the Pacific Plate ($\approx$ N60°W).

The temporal variation of stress state related with the variation of anisotropic properties of the medium can be revealed by the prominent effect of shear wave splitting. The seismic wave characteristics in various directions depend on the symmetry and degree of anisotropy. Under shear wave splitting experimental and theoretical studies, the anisotropy is attributed to the preferential alignment of fluid-filled cracks, pores, and/or minerals under applied stress and belongs to the hexagonal symmetry with the horizontal symmetry axis (HTI; horizontally transverse isotropy) in the crust or to the orthorhombic symmetry in the upper mantle, in general (e.g., Hudson, 1981; Crampin, 1990, 1991; Crampin and Lovell, 1991). Following the HTI model of the medium, the azimuth of fast shear wave polarization (φ) is consistent with the maximum horizontal stress direction (σ_H), which is normal to the symmetry axis. A good correlation among φ, regional tectonic compressional stress direction, and σ_H obtained from shallow event fault plane solutions was reported in a number of papers (e.g., Kaneshima et al., 1987; Kaneshima, 1990). The change in orientation of maximum stress directions should lead to the corresponding change in crack alignment. From rock physics experiments with up to 90 MPa applied stress, Ilchenko and Gorbatsevich (1999) showed the rotation of the symmetry axes (up to 90° for granodiorite samples) in addition to the gradual velocity increase. Dyadkov et al. (2000) revealed evidences for significant temporal changes in the regional stress directions. Based on different geophysical monitoring methods, it was detected that extensional tectonic stress regime changed to compressive regime in the Baikal Rift area during the period of 1992–1993. Concurrently, seismicity became active along the Kuril–Kamchatka and Japan seismic zones located on the opposite side of the Amurian Plate during this 2-year period. Temporal changes in the fast shear wave polarizations around the time of large earthquake occurrences have been reported (Krasnova and Chesnokov, 1998). Slight changes in fast polarization directions (7–10°) were observed due to the hydraulic pumping experiment (Crampin and Booth, 1989). The time delay between split shear waves (δt_{SS}) is more sensitive to the velocity variations with time. The splitting time delay is proportional to the anisotropy degree and the length of travel path within the anisotropic medium (e.g., Liu et al., 1997; Bokelman and Harjes, 2000). Recently, significant amount of data shows the relations between variations in split shear wave time delays and stress changes caused by different processes (e.g., earthquake, volcanic activity, hydraulic pumping). As regards to the seismic process, a general increase in normalized time delays (δt_{SS}) is observed during the time of a large earthquake preparation, when sufficient deformation energy is accumulating over a vast medium volume, and stress builds up. When the energy is released by earthquake, the time delays abruptly decrease after reaching their critical values estimated about 8–12 ms/km in the crust (Crampin, 1998, 1999). For the seismically stable periods, the background values of δt_{SS} are considered to be about 2–4 ms/km.

Since shear waves propagating through the medium interfaces generate converted waves of different types, the shear wave field may be complicated. Some of the converted waves like SP, $SPqS_2$ may leave the direct qS_1-wave behind, and some shear waves (qS_1qS_2, $SPqS_1$,...) may be placed between the direct qS_1 and qS_2 waves. The used shear wave splitting methodologies are mainly based on the four criteria in the split shear wave recognition: (1) polarization orthogonality, (2) particle motion linearity, (3) waveform similarity, and (4) maximum value or ratio of the wave amplitudes (e.g., Shin et al., 1989; Silver and Chan, 1991; Gledhill and Stuart, 1996; Wolfe and Silver, 1998).

Even if all of the criteria satisfy the data well, there might be uncertainty in the choice between split shear wave pairs especially when the time delay expected is much greater than the wave period. At the same time, to our knowledge, there is no assured evidence about the waveform similarity and amplitude ratio between shear waves generated by the earthquakes in anisotropic medium or their dependence from the focal mechanism.

In this paper, we investigate data from local small earthquakes recorded at the Petropavlovskaya seismic station (PET) located in Petropavlovsk–Kamchatski for the seismically active 3-year period of 1996–1998. We present an analysis of shear wave splitting and distribution of splitting parameters in space and time for events of different depth beneath the PET station.

2. Data

The local small earthquakes recorded at PET for the period 1996–1998 are used. The broadband station PET is operated by the Incorporated Research Institute for Seismology (IRIS) and KEMSD GS RAS. Following the regional catalogue of KEMSD GS RAS, the total number of seismic events with $M \geq 5.3$ amounts to about 85 during 1996–1998 (Fig. 1a). Fig. 1b displays the epicenter distribution of seismic events with $M \geq 5$ in the South Kamchatka over the 3-year period. The numbers in the map emphasize the location of the most active areas and general sequencing of their excitations in time. In fact, all large events, except for one, are located at the distances greater than 100 km from the station. The largest Kronotsky Earthquake ($M = 7.7$, 54.95°N, 163.23°E) is located at a distance of 340 km from PET. On January 1, 1996, the strong crustal Karymsky earthquake ($M = 7$) occurred concurrently with the Karymsky Volcano eruption at a distance of 110 km northward PET. Another strong crustal earthquake ($M = 7.1$) occurred in the Avacha Bay at a distance of 200 km on June 21, 1996. The nearest large event ($M = 5.1$) occurred on October 31, 1998 at a depth of 167 km and a distance of 28 km from PET.

For the shear wave splitting measurements, seismic records of events with $M < 3.6$ and the epicenter distances less than 100 km from PET are used. Since crustal seismicity beneath PET is comparatively low, the mantle earthquakes associated with the submerging Pacific Plate prevail in seismic records. The quality of seismic records was inspected and selected based on the signal-to-noise ratio. As a result, records from 287 events were chosen for processing. Data have lack of events within 0–19- and 26–31-km depth intervals. A majority of events (205) is distributed in the depth range from 40 to 184 km. The maximum spectrum amplitudes for shear waves are observed generally in the frequency bands 2–8 and 5–14 Hz for the deep and crustal events, respectively. A band-pass filter (1–20 Hz) was applied to achieve a better signal resolution.

The velocity structure under Kamchatka is defined for P-waves mainly and weakly known for S-waves (e.g., Kuzin, 1974; Gorbatov et al., 1999). Since the 5-km upper layer has a low velocity ($V_p = 3.6$ km/s) relative to the lower one (5.7 km/s), incidence angles of waves have predominantly near-vertical directions at the free surface. It is remarkable that surface waves are not practically observed on the records from the local events. Computations of ray paths of the direct waves from various source locations based on the velocity model show that waves propagated from depths greater than 35 km have precritical incidence angles ($< 33°$ for $V_p/V_s = 1.73$) at the free surface. The effective shear wave window cones for the events from the 10-, 20-, and 30-km depths are estimated as a direct ray path (source–receiver) inclination of about 42°, 67°, and 74°, respectively. Accounting for the lack of data within 0–19 km, the effective shear wave window is estimated as 70°.

3. Data processing

For the assured wave identification and parameter determination, a number of methods are used successively. The data processing based on polarization methods proposed by Galperin (1984) is intended for more accurate analysis of polarization vectors of the waves. We estimate not only parameters of the direct fast and slow shear waves, but also the parameters of direct compressional wave to check the relationship between the three waves.

The data processing starts from the analysis of instantaneous wave polarization defined by transforming the three-component seismograms NEZ to those in

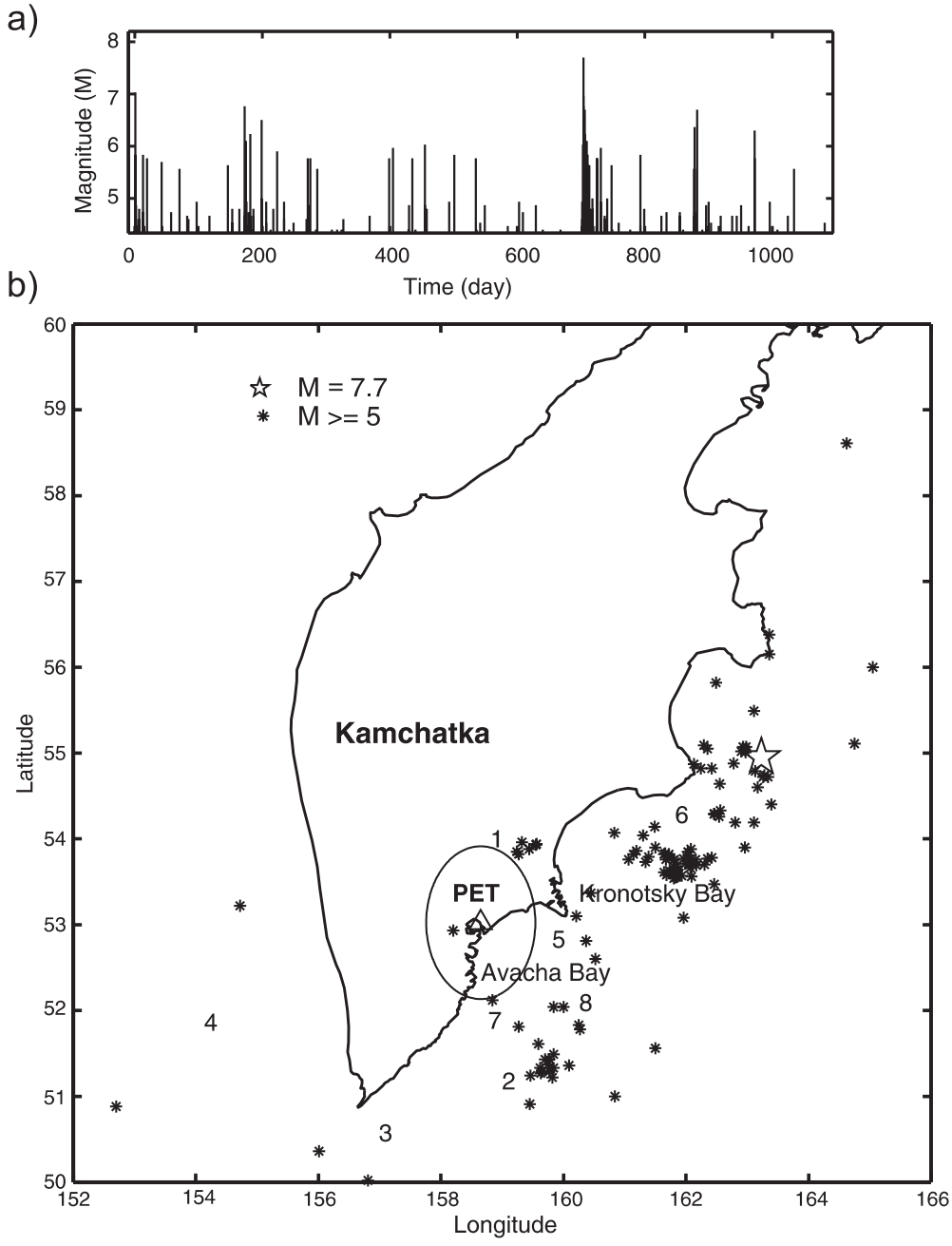

Fig. 1. (a) Distribution of earthquakes of M>4 occurred at south Kamchatka over the 3-year period of 1996–1998. (b) Map of earthquake epicenter locations. An open triangle denotes the location of the IRIS station PET, and circle of 100-km radius denote the study area. An open star denotes the location of the Kronotsky Earthquake (M=7.7, December 5, 1997). Numbers indicate the locations of the most active zones with their excitation time order.

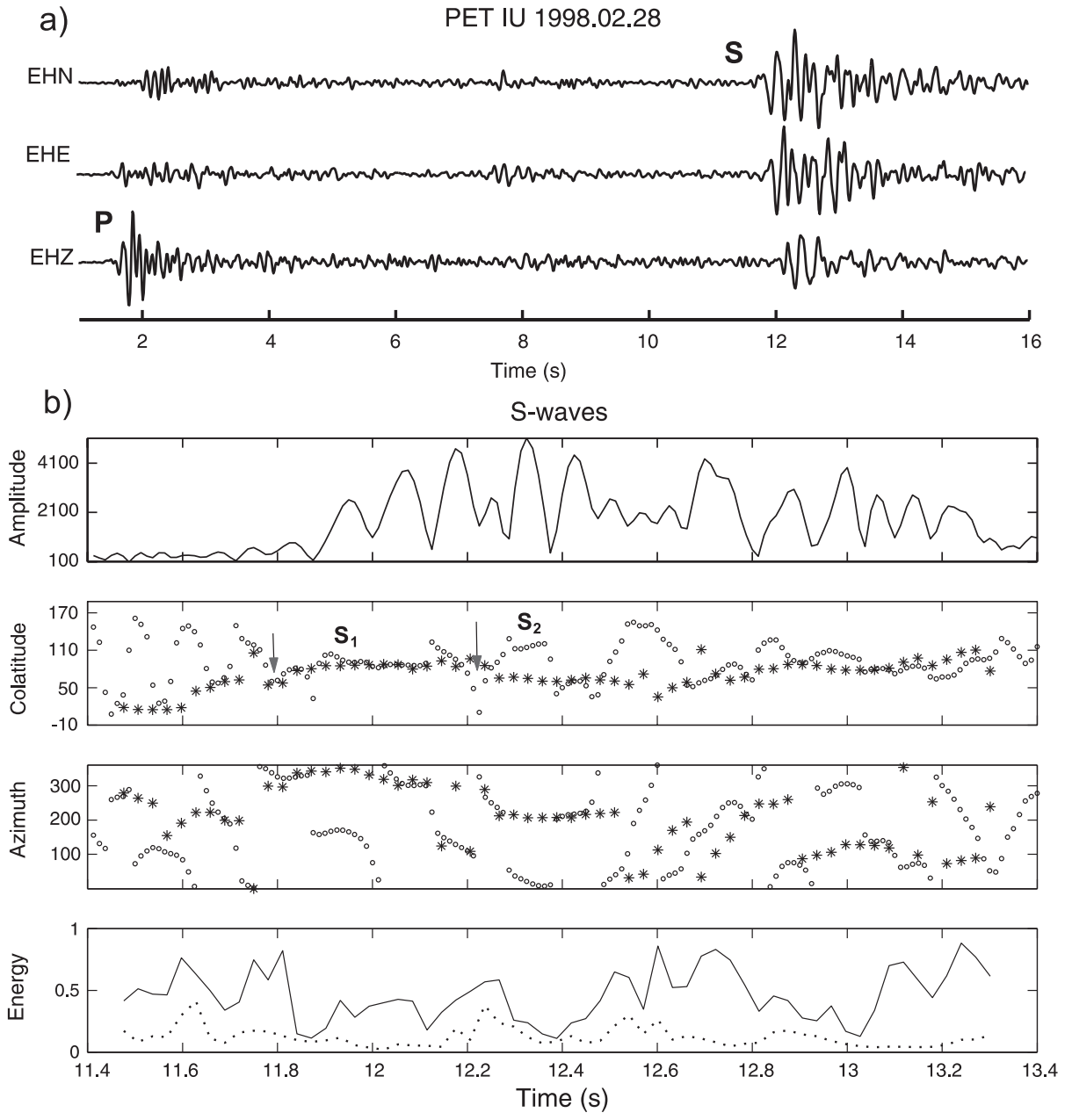

Fig. 2. The three-component seismograms (a) and seismograms constructed in the spherical coordinate system within S-wave time interval (b) for the event occurred on February 28, 1998 with $M = 1.3$, depth $H = 90.8$ km, distance $R_e = 42$ km, and epicentral azimuth $Az = 284°$. Asterisks represent statistical directions of polarization with overlapping moving window (≈ 0.1 s), while open circles represent the instantaneous directions. Arrows indicate prospective onsets of the fast and slow S-waves. Solid and dashed lines are the normalized relative energy along the second and third polarization ellipsoid axes.

the spherical coordinate system $R\theta\varphi$, where $R(t)$ is the amplitude, $\theta(t)$ is the colatitude, and $\varphi(t)$ is the clockwise azimuth from the north. An example of three-component seismograms and seismograms in the spherical coordinate system for the S-wave time arrival interval is presented in Fig. 2. For the linearly polarized wave, the azimuth and colatitude are stable during half a wave period. In accordance with the wave type, the values of $\varphi(t)$ or $\theta(t)$ may jump sharply when the displacement direction changes by 180°. In the case of circular polarization (two shear waves with orthogonal polarizations interfere with small phase shift), $\theta(t)$ undulates relative to the genuine value, and $\varphi(t)$ changes smoothly within 360° angle interval. The sharp alteration in $\theta(t)$, $\varphi(t)$ indicates the change of wave type. When waves interfere, the behavior of azimuth and colatitude curves may be complicated and depends on the interrelation among amplitudes, polarization directions, and time delays of the interfering waves.

The statistical distribution of polarization vectors in space (polarization ellipsoid) is analyzed for the given time intervals. Three principal axes of polarization ellipsoid are determined by the eigenvectors X_k and eigenvalues λ_k of the covariance matrix for displacement vectors $\mathbf{u}(n,e,z,t)$. The eigenvector X_1 corresponding to λ_1 indicates the statistical wave polarization direction. For the practical purpose, X_1 is converted to the spherical coordinates $(\bar{\theta},\bar{\varphi})$. The eigenvalues λ_k define relative energy along the polarization ellipsoid principal axes. The eigenvalues are ordered and normalized by the largest one ($\lambda_1 = 1 \geq \lambda_2 \geq \lambda_3$). The normalized eigenvalues λ_2 and λ_3 indicate the wave linearity degree and, hence, the interference effect: the smaller the values of λ_2 and λ_3, the higher the linearity degree of oscillations. Firstly, statistical polarizations $\bar{\theta}(t)$, $\bar{\varphi}(t)$, and ellipsoid axes $\lambda_2(t)$, $\lambda_3(t)$ are calculated within overlapping moving time window and analyzed together with the instantaneous polarizations $\theta(t)$, $\varphi(t)$ (Fig. 2b). On later steps of data processing, estimation of statistical polarization directions and ellipsoid axes are applied to the arbitrary chosen time intervals. In Fig. 2b, prospective qS_1 and qS_2 are distinguished at time intervals of about 11.9–12.2 and 12.2–12.5 s based on the stabilizing $\theta(t)$, $\varphi(t)$ and/or $\bar{\theta}(t)$, $\bar{\varphi}(t)$ and decreasing $\lambda_2(t)$, $\lambda_3(t)$. In the time interval of around 12.2 s, an interference effect between qS_1 and qS_2 waves is observed. As could be seen in Fig. 2b, qS_1-wave is disturbed by another shear wave with an earlier arrival, smaller amplitude, and close colatitude and azimuth values. The best oscillation linearity refers to time around 11.85, 12.4 (qS_2), and 13 s. Following the analyses of instantaneous and statistical polarizations, the azimuth and colatitude of prospective P, qS_1, and qS_2 waves are picked up manually. This procedure allows us to recognize phases and define their polarization vectors with good accuracy.

At the next step, the method of polarization seismograms (or multicomponent vector seismograms) is applied to analyze wavefield patterns in space and to distinguish waves of various types based on their polarizations. Polarization seismograms are constructed as projections of displacements on a chosen set of unit vectors $\{\mathbf{l}(\varphi,\theta)\}$.

$$u_l^p(t) = (\mathbf{u}(n,e,z,t)\cdot\mathbf{l}(\varphi,\theta))^m. \quad (1)$$

The parameter $m>1$ is responsible for the radiation directivity and allow more energetic regular phases be emphasized suppressing the noise effects. Since the incidence angles of rays at the free surface are close to the vertical direction in the study area, for practical purposes, polarization seismograms are constructed in the horizontal plane for the S-waves and in the vertical incident plane for the P-wave. Fig. 3a presents polarization seismograms for S-wave time interval with the 10° azimuth step counted clockwise from the north. As could be clearly seen in Fig. 3a, qS_1- and qS_2-phases marked have maximal amplitudes and show a good linearity (neighboring phases form straight and parallel lines with azimuth increase) and a good

Fig. 3. (a) Polarization (vector) seismograms constructed with the directivity parameter $m=2$ in the horizontal plane for the time interval of the S-waves. Arrows indicate fast (S_1) and slow (S_2) shear waves, and converted shear wave (S_c) as well traced in the very first arrival. (b) Particle motion of shear waves projected onto the horizontal plane NE for the time interval 12–12.5 s. (c) Seismograms of P, S_1, and S_2 waves projected on the directions corresponding to their polarization vectors. On the seismogram of S_1 wave, dotted line indicates phases of S_2-wave moved backward on the estimated time delay between split waves (0.2625 s). Correlation coefficient between shear waveforms is estimated to be about 0.8196. The data used are the same as those in Fig. 2.

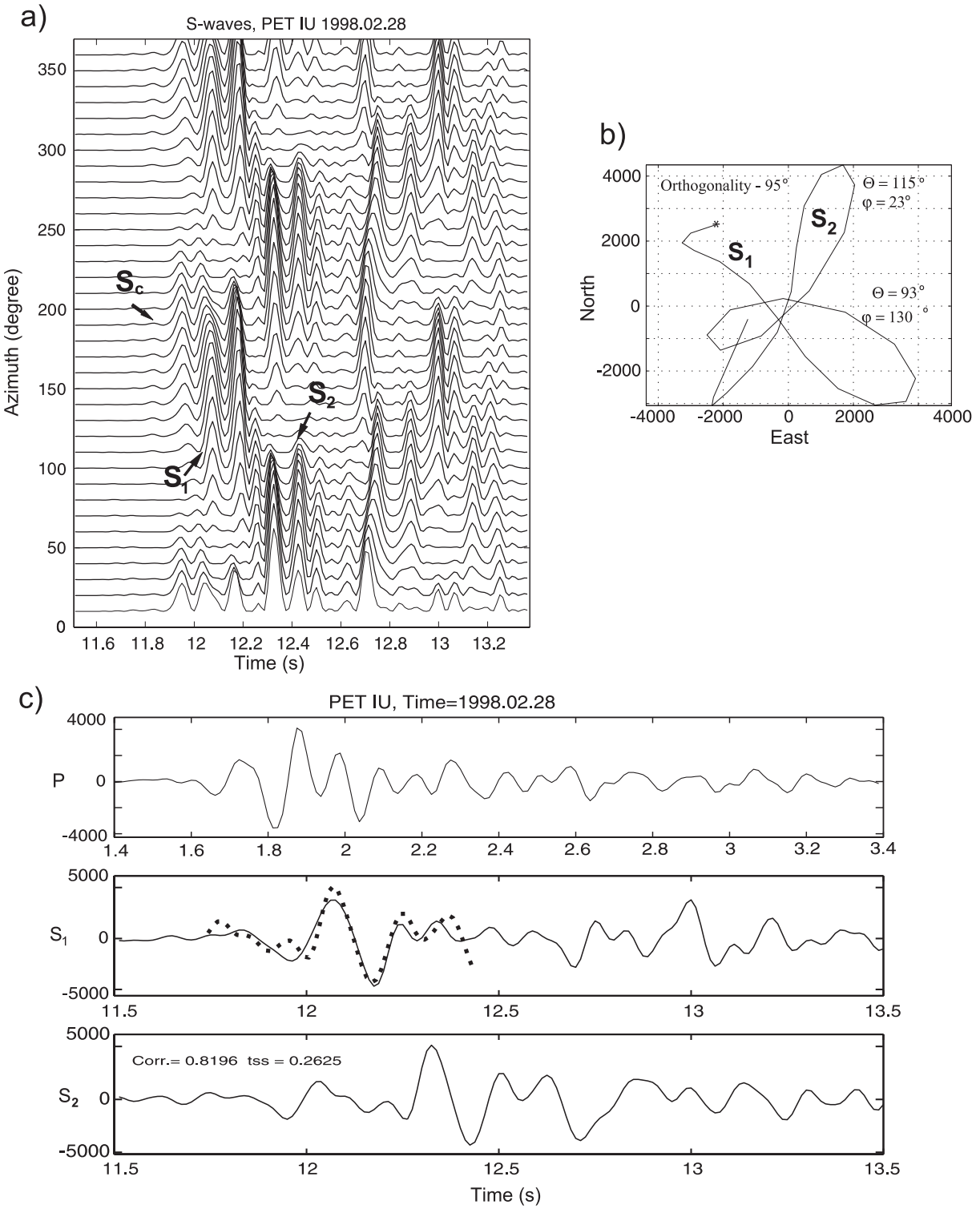
a)
S-waves, PET IU 1998.02.28
Azimuth (degree)
Time (s)
S_c
S_1
S_2
b)
Orthogonality - 95°
Θ = 115°
φ = 23°
Θ = 93°
φ = 130°
North
East
c)
PET IU, Time=1998.02.28
P
S_1
S_2
Corr.= 0.8196 tss = 0.2625
Time (s)

orthogonality as well. Other phases, which are observed at azimuths closer to either qS_1 or qS_2 azimuth, have smaller amplitudes and are considered as converted waves. A converted wave marked in Fig. 3a as S_c is traced in the very first arrival with a greater azimuth than that for qS_1-wave.

To estimate polarizations, amplitudes, and time delays of split shear waves, the following parameters are picked up manually from the polarization seismograms: (1) the qS_1 and qS_2 onsets t_{S1}, t_{S2}; (2) time intervals Δt_{S1}, Δt_{S2} where each shear waveform is expressed best; (3) time interval Δt_{S12} comprising both the shear waves. For the time intervals Δt_{S1} and Δt_{S2}, statistical polarizations (θ,φ,λ_2,λ_3) and maximum amplitudes of the fast and slow shear waves as well as orthogonality between wave polarizations are calculated. The statistical polarizations are estimated also for the time interval Δt_{S12} in which two principal displacement directions indicate polarizations of the S-waves, and the direction normal to them is expected to be the P-wave polarization direction. Particle motion projections on the coordinate planes are constructed for all time intervals chosen. Fig. 3b displays an example of the particle motion of split shear waves in the horizontal plane in the time interval Δt_{S12}. The splitting time delay is estimated as a difference between the qS_1 and qS_2 onsets ($\Delta t_{SS} = t_{S2} - t_{S1}$) and based on the cross-correlation between polarization components in the time interval Δt_{S12}. The splitting time delay is accepted following the highest cross-correlation coefficients (≥ 0.75). This method yields a good result if shear wave polarizations are close to horizontal directions, and if there is a good similarity between shear waveforms.

After application of different methods, we get a set of S-wave polarization directions and time delays between split S-waves. The optimal parameters are chosen under the criteria satisfying wave linearity, orthogonality, and waveform similarity between the waves. The final result is accepted after the inspection of seismograms for P-, qS_1-, and qS_2-waves projected along their polarization directions and calculation of cross-correlation function between shear waveforms with the final splitting time delay estimation (Fig. 3c). Thus, the optimal result of wave parameter estimations for the chosen record are shown in Figs. 2 and 3 and can be presented as follows: (1) qS_1-wave: polarization (θ,φ), (87°, 308°); linearity (λ_2, λ_3), (0.34, 0.06); (2) qS_2-wave: polarization, (115°, 23°); linearity, (0.19, 0.16); (3) qP-wave: polarization, (5°, 75°); linearity, (0.14, 0.03); (4) space angles between wave polarization vectors: $\gamma_{S1S2} = 95°$, $\gamma_{S1P} = 91°$, $\gamma_{S2P} = 112°$; (5) S-waveform correlation coefficient, 0.8196; (6) splitting time delay, 0.2625.

The errors in shear wave parameter measurements may be estimated in some ways. Since we use a set of different approaches to define wave polarization, the physical resolution is estimated about 5–10° in azimuths if half or one wave period is well observed. If a shear wave is superimposed by another signal the accuracy may be reduced to 20–30° depending on the signal-to-noise ratio. In general, the estimated error appears to be 10–20° by using various methods for different wave phases. In fact, errors in polarization vector are estimated in terms of polarization ellipsoid axis values for the chosen wave phase as $\varepsilon_I \approx \arctan(\lambda_2)$ in the incidence plane and $\varepsilon_\perp \approx \arctan(\lambda_3)$ in the normal plane. Thus, the polarization resolution is higher, when values of λ_2 and λ_3 are smaller. Following this, the polarization vectors are defined (Fig. 3) for the qS_1-, qS_2- and qP-waves with errors (ε_I, $\varepsilon_\perp$)–(18°, 3°), (11°, 10°), and (8°, 1.7°), respectively. The source of errors in time delay measurements connects with the uncertainty shear wave onsets when one or both waves are traced in later arrivals. For the interfering shear waves, the error is estimated from a quarter up to half a period. If split shear wave are separated, but their first phases are distorted by other signals, the error may reach one period.

The seismic records have been processed expecting that direct waves propagate from the source as the strongest ones and have maximum amplitudes. In some records, pronounced split shear waves of weaker amplitudes are traced in the very first arrivals. Most of these waves may be generated at the crustal or lower interfaces as converted $SPqS_i$ or refracted (head) $SPqS_i$ and $SSqS_i$-waves and arrive prior to the direct shear waves. The top row in Fig. 4 displays polarization seismograms in which the direct shear waves are traced in the first arrivals, while the seismograms with small-amplitude converted waves (S_c) shown in the bottom row are traced first. The S_c-waves have weaker amplitudes comparable to the waves traced in the later arrivals and display a good waveform similarity, good orthogonality, and they are well separated from each other. The polarization azimuths

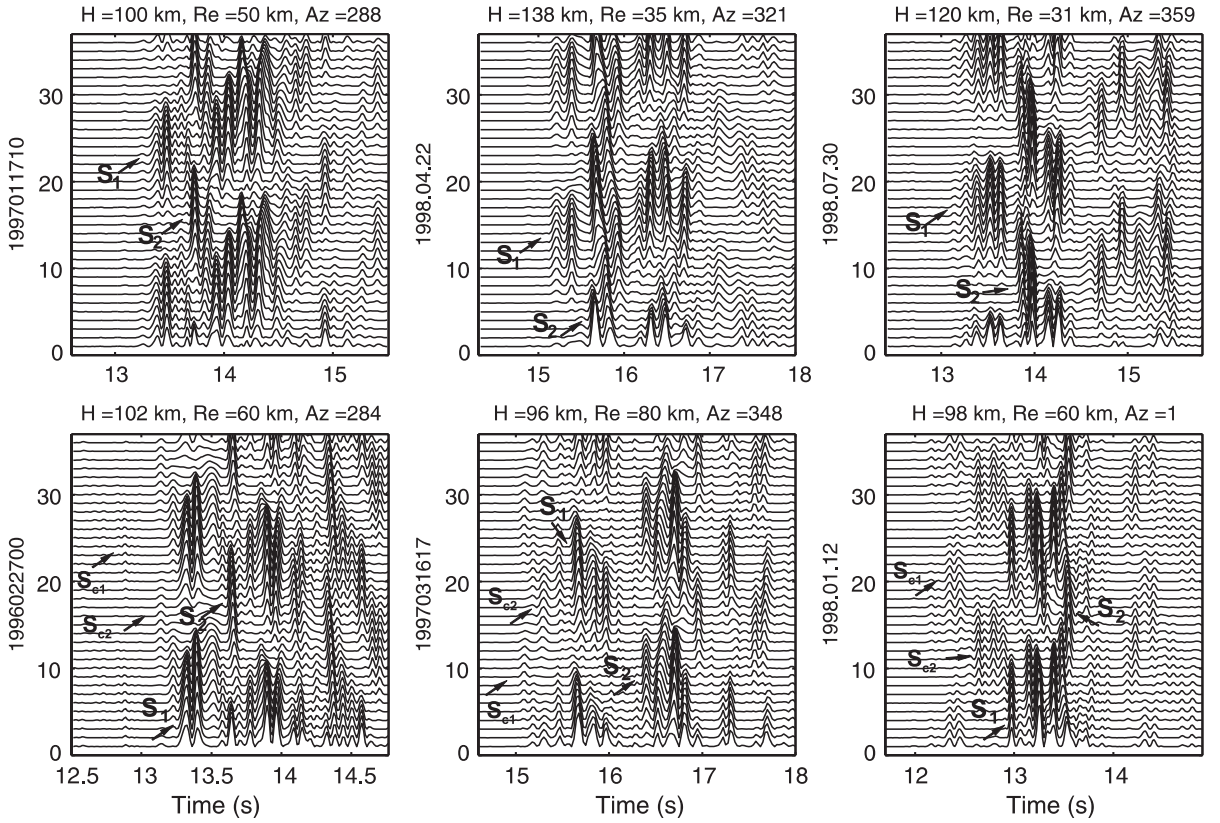

Fig. 4. Examples of polarization seismograms when either maximum amplitude direct (S_1,S_2) or small-amplitude converted (S_{c1},S_{c2}) split shear waves are traced in the first arrivals. The polarization seismograms are constructed with the directivity parameter $m=2$ in the horizontal plane with the 10° azimuth step counted clockwise from the north. Earthquake focal depth (H), epicentral distance from PET (R_e) and azimuth (Az) are indicated at the top of each seismogram set. Earthquake origin time is indicated at the left side of each seismogram set.

of the fast small-amplitude waves may or may not be similar to those for the fast waves with maximum amplitudes. For the events dated February 27, 1996 and January 12, 1998, the polarizations of the fast direct and converted phases are similar, while for the event that occurred March 16, 1997, they are almost normal to each other. As could be clearly seen in Fig. 4, the split direct shear waves do not always reveal good similarity in their waveforms.

4. Results and analysis

4.1. Fast shear wave polarizations

Fig. 5a presents the distribution of azimuths of the direct fast S-wave polarization and back-azimuths for all events analyzed. For statistical purposes, the directivity is ignored in S-wave azimuths ($\varphi \pm 180°$). Polarization azimuths and back-azimuths used commonly throughout this paper are measured clockwise from the north. The colatitudes in S-wave polarizations analyzed are distributed in the range of 65–125°, predominantly within 80–110°, and those for P-waves have precritical angles (35°). The majority of event back-azimuths is located eastward from PET with prevalent directions N100–140°E. The dominant directions φ lie within N80–110°E. Statistical estimates give the mean value of the fast S-wave azimuths equal to 92.4° with a standard deviation about 37.2° for the 3-year period 1996–1998. The data misfit amounts to about 2% for the 95% and 68% confidence intervals of normal distribution. The increased number of anomalous φ is detected within 0–40° azimuth range.

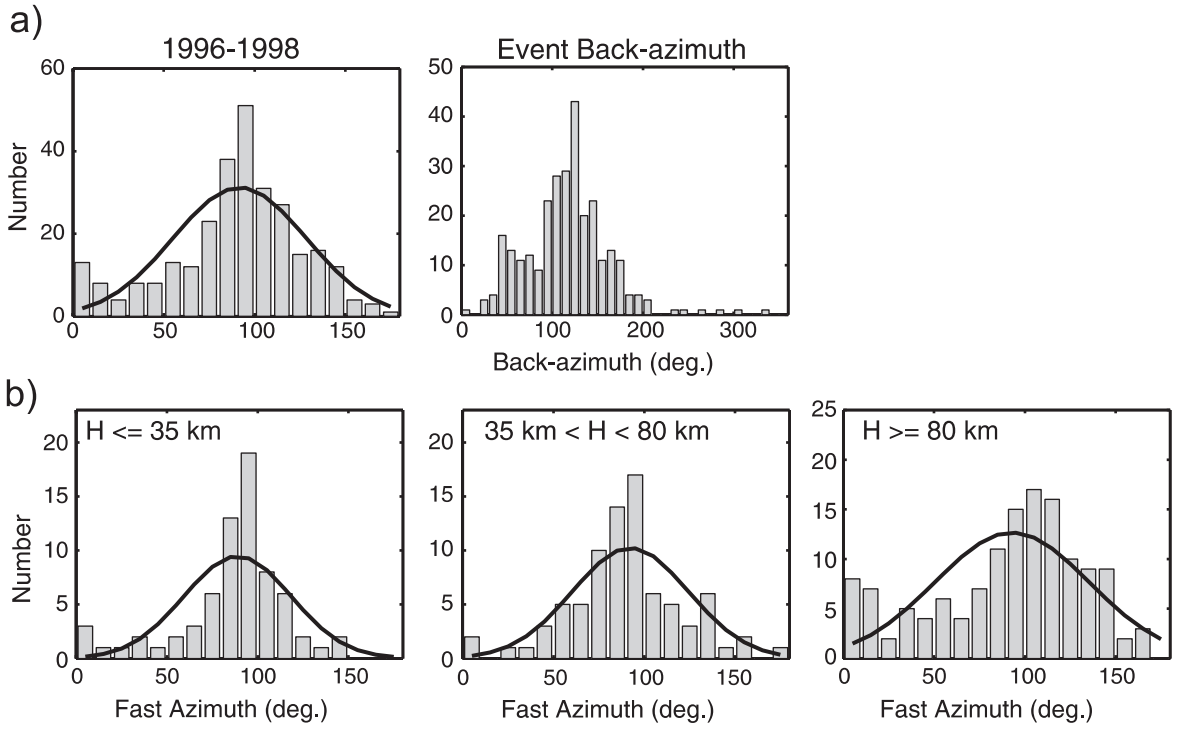

Fig. 5. (a) Distributions of polarization azimuths for the fast S-wave and event back-azimuths over the 3-year period of 1996–1998. (b) Distributions of fast S-wave azimuths for events of three depth intervals over the 3-year period. Gaussian approximation of the fast azimuths is plotted by the solid line on the histograms.

Shear wave azimuths for events of different focal depths show some diversity in their distribution over the 3-year period. The crustal ($H \leq 35$ km) and intermediate depth ($35 < H < 80$ km) earthquakes give similar dominant azimuths about 80–100°, while the deep earthquakes ($H \geq 80$ km) yield the dominant azimuths in a broader range 80–150° (Fig. 5b). For the deep events, the increased numbers of fast S-wave azimuths in the intervals 0–30° and 140–150° were also observed.

The observed polarizations were examined with the theoretical polarizations for the transversely isotropic and orthorhombic media of various orientations. The polarizations computed for the HTI model with the symmetry axis oriented to N15 ± 10°E and a possible dipping angle ± 10° are in the best accordance with the observed data. Fig. 6 displays the theoretical and observed fast shear wave polarizations mapped on the horizontal plane. Theoretical polarizations are calculated for homogeneous HTI medium with the symmetry axis directed to N20°E. In the model, P- and S-wave velocities are equal to 6.5 and 3.6 km/s, respectively, which are close to the average crustal velocities of Kamchatka, and shear wave anisotropy coefficient reaches the value of about 6% in the symmetry plane normal to the horizontal symmetry axis. The elastic parameters of TI medium are constructed for the model of homogeneous fractured medium proposed by Aizenberg et al. (1974) and Hsu and Schoenberg (1993). Following Liu et al. (2000), the fractured medium is equivalent to the cracked medium studied by Hudson (1981).

Since in the theoretical model the qS_1- and qS_2-wave surfaces intersect each other, the sharp change of polarization could be clearly seen in the southern and northern areas (Fig. 6a). The back-azimuths and colatitudes of observed data are localized mainly in the area where qS_1-wave arrives earlier than qS_2-wave (Fig. 6b and c). Only 14 events (5%) are located in the area where qS_2-wave arrives earlier. The fast azimuths in this area show a good agreement with the computed azimuths for six events giving an azimuth difference

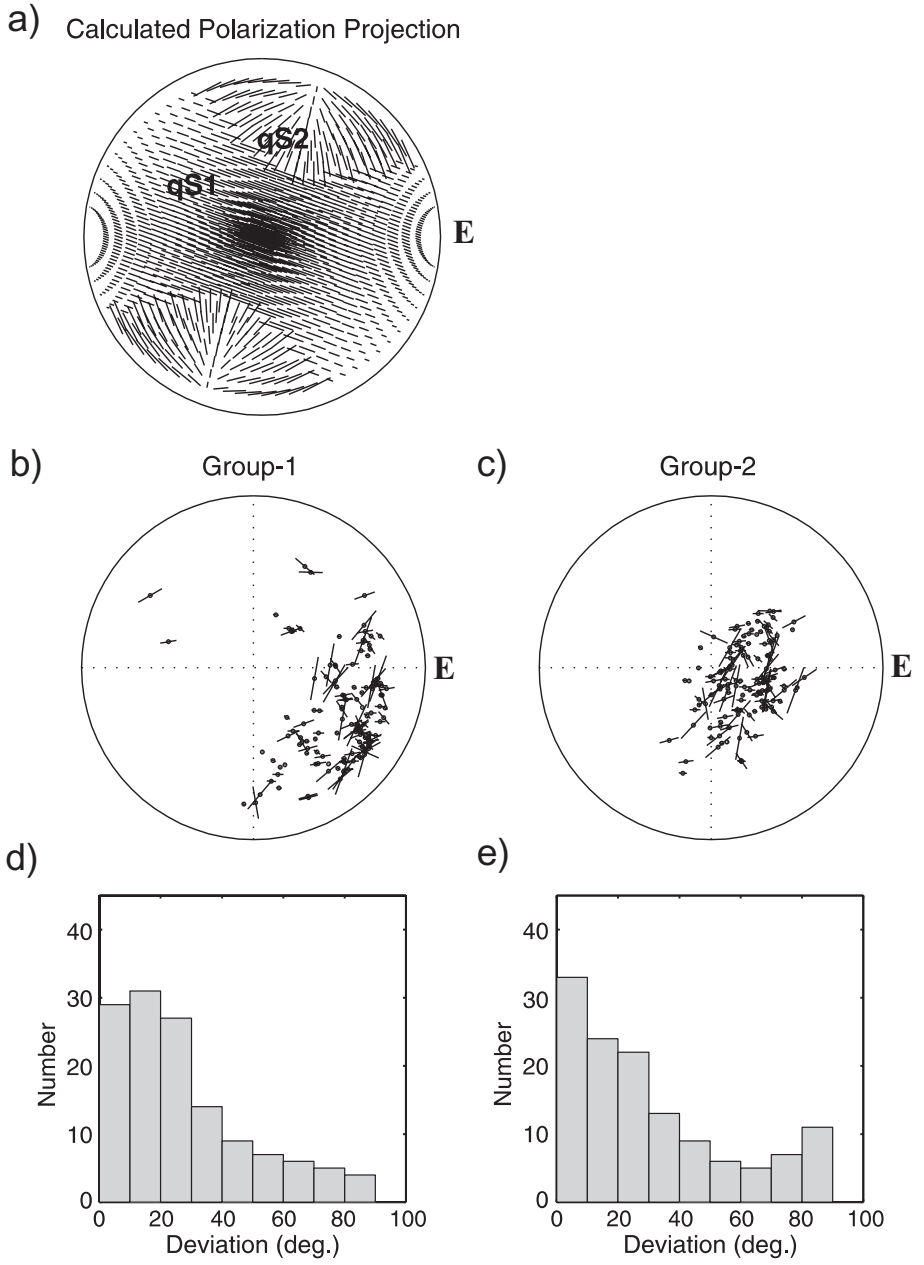

Fig. 6. (a) Theoretical fast S-wave polarizations at various ray azimuths and incidence angles (φ,θ) are projected onto the horizontal plane. The theoretical polarizations are calculated for the HTI model with the symmetry axis oriented to N20°E and anisotropy coefficient of 6%. The large circle corresponds to the contour of ray incident angles of 90°. (b and c) Observed fast S-wave azimuths are mapped with respect to PET onto the horizontal plane for events with depths upper 80 km (Group 1) and lower 80 km (Group 2), respectively. The azimuth lengths are proportional to the deviations from the predicted ones at the same locations. The large circle corresponds to the contour of ray incident angles of 90°. (d and e) Histograms of fast S-wave azimuth deviations for events of Groups 1 and 2, respectively.

less than 30°. For three events, the azimuth difference exceeds 60°. This small amount of data does not allow us to determine surely whether the intersection between shear wave surfaces exists or not.

The deviations between theoretical and observed fast azimuths $\Delta\varphi = |\varphi - \varphi_T|$ at the same locations were estimated. The dominant number of azimuths (63%) shows the deviations less than 30°. The amount of anomalous azimuths ($\Delta\varphi \geq 60°$) gives 2.8%, 3.8%, and 9.7% for the crustal, intermediate, and deep events, respectively. The proposed HTI model fits especially well the data for the events with back-azimuths 80–130° giving about 5% of anomalous data. For these back-azimuths, the sampling presents 46% of data. In other directions, events are distributed more sparsely.

Fig. 6b and c displays fast S-wave azimuth deviations for the event depths up to 80 km (Group 1) and lower than 80 km (Group 2). Statistical distributions of φ for the crustal and intermediate events show close results and satisfy well the HTI model proposed giving 65.5% of dominant deviations with $\Delta\varphi \leq 30°$ and 10.3% with $\Delta\varphi \leq 60°$. For the deep events, the number of anomalous fast azimuths reaches 17.7%, and the number of dominant deviations with $\Delta\varphi \leq 30°$ accounts for 60.6%. As could be clearly seen in Fig. 6b and c, the polarization projections for Groups 1 and 2 occupy areas which slightly intersect: majority of deep events are localized up to 40° of ray path inclinations, while those for shallower events are distributed mainly within 40–70°. This fact produces difficulties in comparison to polarizations between the groups.

Analysis of anomalous fast azimuth nature shows that it does not clearly depend on either angle of ray path inclination (α_r) or back-azimuth. The anomalous fast azimuths for deep events are scattered almost evenly at various ray path directions. For example, the relative amount of anomalous fast azimuths for deep events within $\alpha_r < 20°$ gives a higher value (22.9%). Fig. 7 shows the distribution of observed S-wave azimuths with back-azimuth for each group. Though the data are distributed uniformly in a broad fast azimuth range, the higher scattering is observed for the deep events within back-azimuth intervals 30–60° (N–NE) and 150–200° (SSE–S). Anomalous azimuths for the crustal events correspond mainly to the east back-azimuths (110–130°). In general, φ are distributed almost symmetrically relative to the back-azimuths 100–120° (Fig. 7). The last agrees with the P-velocity structure from tomographic images (Gorbatov et al., 1999), which do not reveal sure structural asymmetry in the PET area relative to the trench-normal direction. It is expected that the discrepancy in φ relative to the trench-parallel direction is related to the westward-dipping slab and to the

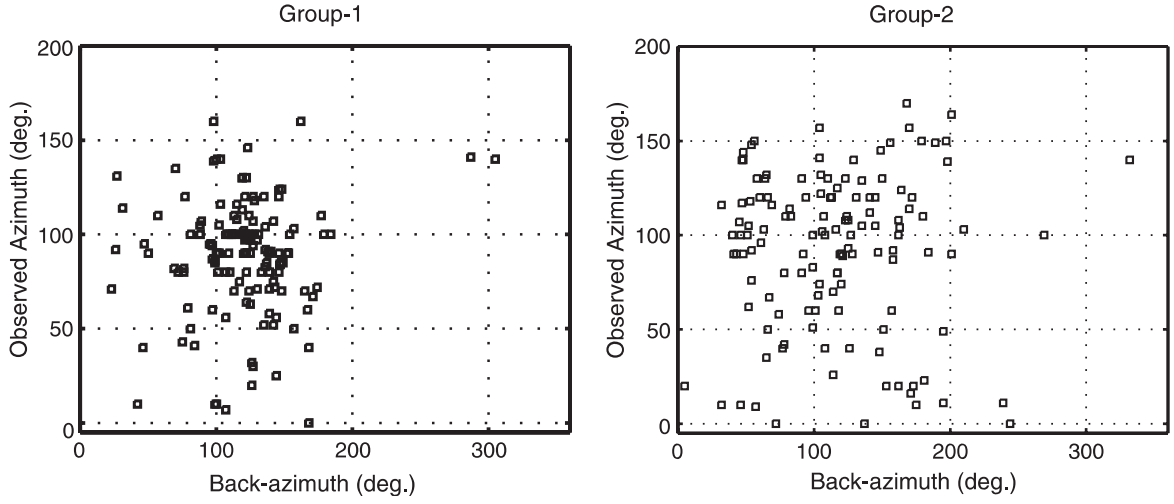

Fig. 7. Distribution of fast S-wave azimuths with event back-azimuth for the events of Group 1 ($H < 80$ km) and Group 2 ($H \geq 80$ km) over the 3-year period.

East Kamchatka Volcanic Belt. Beneath the volcanic front, the low-velocity zone is clearly defined from the upper crust to a depth of 100–150 km. However, the number of events from the western hemisphere is too small for analysis.

We have examined also alternative orthorhombic models for the fast S-wave azimuths of deep events. Fig. 8a present theoretical fast shear wave polarizations for the deep events ($H \geq 80$ km) mapped on the horizontal plane with the fast a-axis oriented to N60°W and 20° from the vertical axis. In this model, the slow b- and c-axes are oriented eastward and northward, respectively. Qualitatively, the distribution of the theoretical fast directions shows an agreement with the observed data. The relative amounts of azimuths with $\Delta\varphi \leq 30°$ and $\Delta\varphi \leq 60°$ represent 49% and 17%, respectively. These statistical results for the orthorhombic model do not differ much from those for the HTI model. At the same time, the dominant azimuth deviations belong mainly in the interval $\Delta\varphi \leq 10°$, and azimuth deviations in other intervals (10–70°) are distributed more evenly. In general, we cannot reject the orthorhombic model from our consideration, but we think that data comparison for HTI model gives clearer statistical result. In addition, we may assume that main changes of

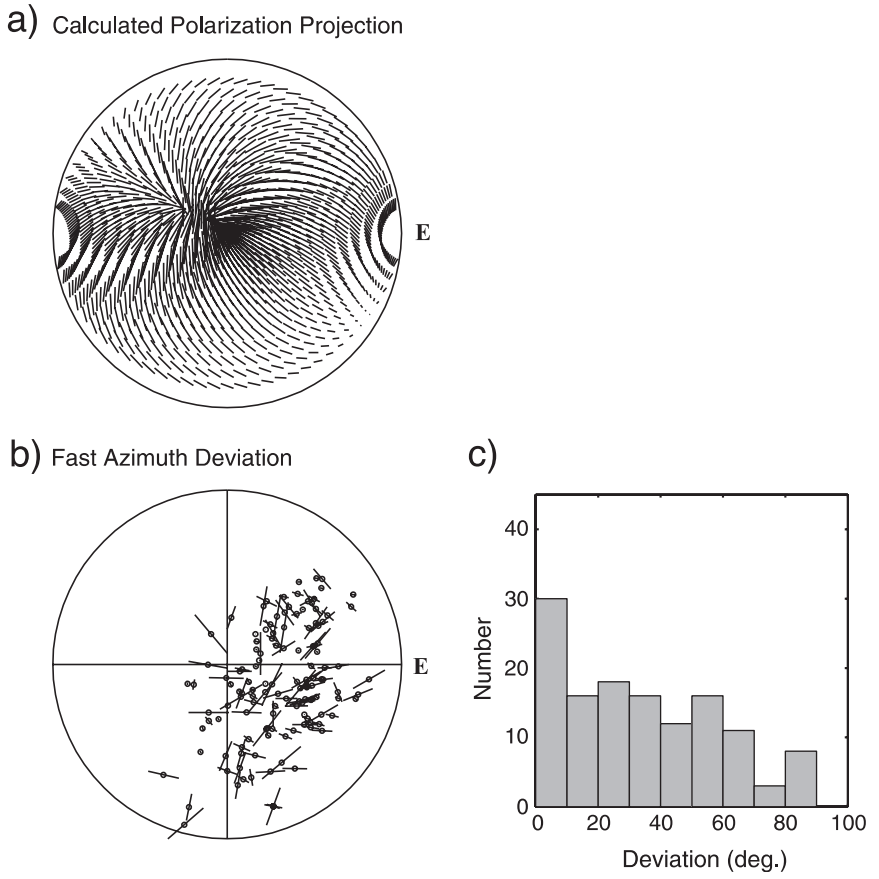

Fig. 8. (a) Theoretical fast S-wave polarizations at various ray azimuths and incidence angles (φ,θ) are projected onto the horizontal plane. The polarizations are calculated for the orthorhombic model with the fast symmetry a-axis oriented to N60°W and 20° from the vertical axis. The slow b-axis and c-axis are oriented eastward and northward, respectively. The large circle corresponds to the contour of ray incident angles of 90°. (b) Observed fast S-wave azimuths for deep events ($H \geq 80$ km) are mapped onto the horizontal plane with the length proportional to the deviations from the predicted ones at the same locations. The large circle corresponds to the contour of ray incident angles of 60°. (c) Histogram of fast S-wave azimuth deviations.

polarization of S-waves generated from the deep events occur in the upper layers in accordance to their wave frequency. The polarization of waves with lower frequency might alter less and satisfies better the orthorhombic model. Unfortunately, based on our records, the sure S-wave polarization dependence on the frequency is not found.

4.2. Time delays between split shear waves

Since the time delays between split shear waves depend on the event location and the anisotropic properties of the media, the time delays were normalized by the hypocentral distance ($\delta t_{SS} = \Delta t_{SS}/R$) representing the delay between split waves per km. Following the HTI model (e.g., Zatsepin and Crampin, 1997), the time delays should have maximum values and more stable behavior for any incidence angle in the band at about $\pm 15°$ to the symmetry plane (P) corresponding to the crack strike. Theoretically, δt_{SS} decrease gradually from the plane P in directions along the symmetry axis. If there exist shear wave intersection or S-wave surfaces approach to each other, δt_{SS} tends to zero at that area and then increase. Based on this, the data were analyzed in two bands at $\pm 15°$ (Band 1) and $15-45°$ (Band 2) to the plane P oriented along 110°.

Fig. 9a and b displays the observed normalized time delays projected onto the horizontal plane in accordance to their ray directions within Bands 1 and 2,

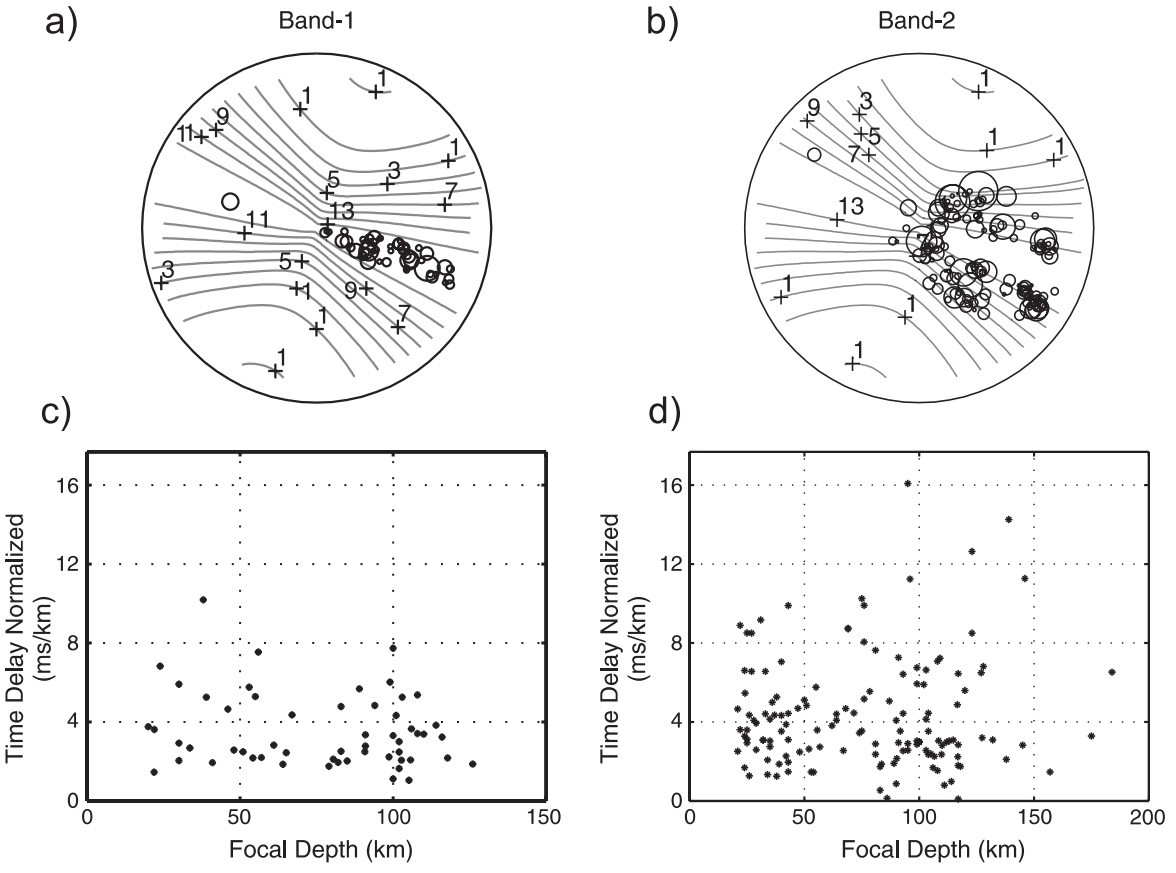

Fig. 9. Distribution of observed normalized S-wave time delays over the 3-year period in the bands at $\pm 15°$ (Band 1) and $15-45°$ (Band 2) to the crack strike, respectively. (a and b) Projections at various ray azimuths and incidence angles onto the horizontal plane. The circle radii are proportional to the time delays. The large circle corresponds to the contour of ray path angles of 90°. Contour plot shows the calculated normalized S-wave time delay distribution for the HTI model as for Fig. 6a. (c and d) Variation of normalized time delays with focal depth.

respectively. Contour plots show the calculated normalized time delays projected onto the horizontal plane for the HTI model with the physical properties mentioned above. Observed δt_{SS} are shown by circles whose radii are proportional to δt_{SS} values. The time delays are scattering almost independently on the event location. There are exceptions for the 40–60° and 135–150° back-azimuth intervals (Band 2), where the largest δt_{SS} are observed. This effect could be clearly seen in Fig. 9b, where increased time delays are localized along the two nearly orthogonal back-azimuth intervals. Note that these back-azimuth intervals correspond to those with the increased scattering of fast S-wave polarizations.

Fig. 9c and d display the variation of normalized time delays with focal depth in the two bands. In both bands, the normalized time delays are distributed almost uniformly. The large δt_{SS} values (>11 ms/km) correspond to events from 90- to 150-km focal depth interval. The mean and standard deviation of δt_{SS} are determined to be about 3.5 and 1.9 ms/km in Band 1 and about 4.3 and 2.8 ms/km in Band 2, respectively. About 5% of δt_{SS} exceed the 95% confidence interval for both the bands.

In general, estimated anisotropy coefficients give low average values about 1%, 1.6%, and 1.8% for crustal, intermediate, and deep depth intervals, respectively, due to a broad scattering in time delays. Anisotropy coefficient is defined for each event as a ratio of split shear wave time delay to the fast shear wave travel time ($\alpha = \Delta t_{SS}/t_{S1}$). The maximum α values up to 7.5% correspond to the events from 90 to 140 km focal depths. The largest α value for intermediate events does not exceed 4%. The data analysis shows also that the chosen HTI model with the 6% anisotropy coefficient corresponds, to a great extent, to the increased observed time delays (Fig. 9).

4.3. Shear wave field

In order to understand better the source of variations in splitting parameters, the shear wave fields for events of close locations or those that occurred at close times were analyzed. Shear wave field is considered as a superposition of the direct and converted waves including multiples generated at the boundaries in the media. The velocity structure of the Kamchatka subduction zone is modelled by the three-layer crust with boundaries located at depths 4–5, 15, and 35 km and the subducting slab dipping westward from 90- to 140-km depths beneath the Petropavlovsk–Kamchatski area (Kuzin, 1974; Gorbatov et al., 1999). In the upper mantle, two layers may be distinguished with boundaries at depths of 60 and 75 km. Assuming that all layers own anisotropy properties, a set of 5–10 converted shear waves is expected to be in the records of the deep events. The amplitudes of converted waves of SP, SPS type and multiples are expected to be quite smaller than those of the transmitted waves. Some intensive converted waves may be also generated at the non-welded contacts which might be represented as mechanically weakened thin layers such as cracked and/or fractured zones, which do not reveal a significant velocity discontinuity (Aizenberg et al., 1974; Schoenberg, 1980; Yanovskaya and Dmitrieva, 1991; Luneva and Young, 1995).

Fig. 10 represents examples of shear wave field observed for the couple events with different hypocenter parameters but happened on the same day. Polarization seismograms dated August 16, 1996 demonstrate a good similarity between shear wave patterns within the first seconds for the crustal and deep events with different azimuths (top row, framed area). Fast azimuths for the events are determined as 100° and 89°, respectively. The fast waves of the events are represented by a long train, while the slow waves are represented by a short impulse. In addition, a good similarity is observed for the crustal and deep events that occurred on March 10, 1997 (third row). In the records, a small-amplitude wave (S_c) with the azimuth normal to the fast azimuth of the direct wave is traced ahead of the direct wave arrival time. For the crustal event, S_c-wave is detected clearer and better separated from S_1-wave. Fast azimuths have anomalous values of 190° and 195°, and time delays are estimated about 1.74 and 0.81 s, respectively. The observed anomalous parameters might be related with the large earthquake ($M = 5.2$) that occurred a day later in the south area of the Avacha Bay (March 11, 1997).

Shear wave patterns for the deep events dated November 18, 1996 (second row, Fig. 10) show a good agreement in the fast S-wave directions ($\varphi = 100°$ and $\varphi = 117°$, respectively), but a significant difference is observed in the fast S-waveforms and in the number of waves generated at the medium

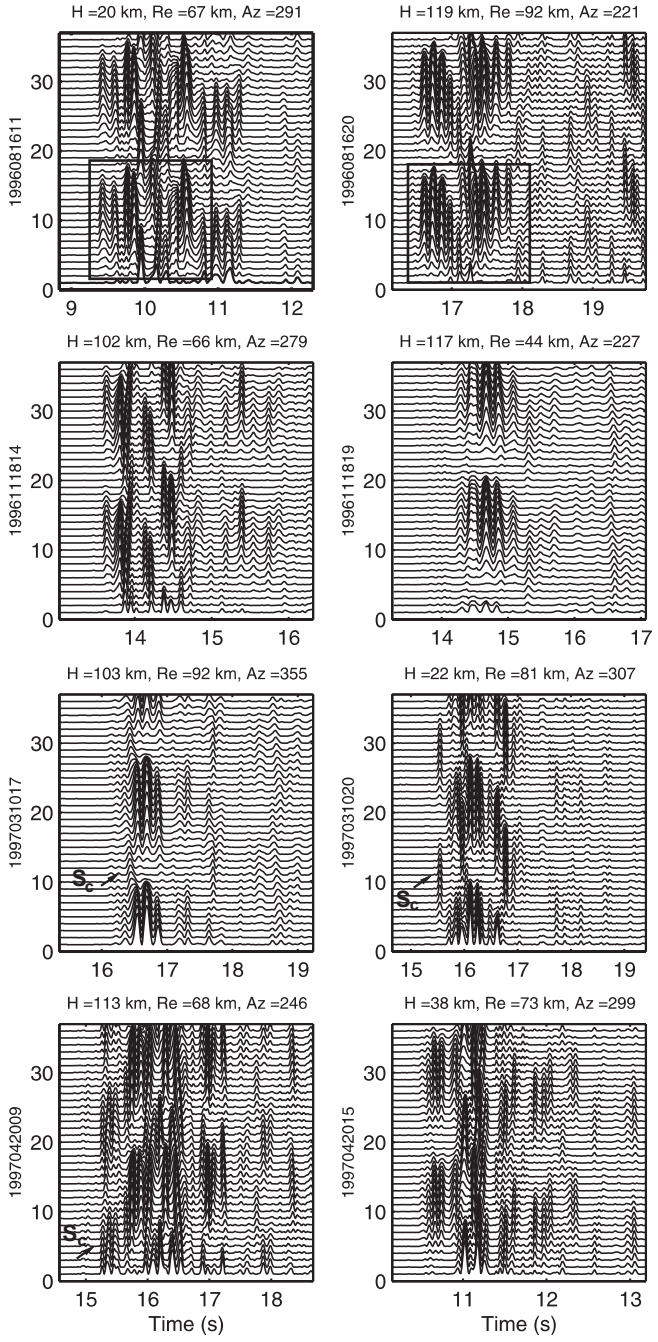

Fig. 10. Polarization seismograms demonstrate shear wave fields and splitting effect for the pairs of events that occurred on the same day. Earthquake focal depth (H), epicentral distance from PET (R_e) and azimuth (Az) are indicated at the top of each seismogram set. Earthquake origin time is indicated at the left side of each seismogram set. The polarization seismograms are constructed with the directivity parameter $m = 2$ in the horizontal plane with the 10° azimuth step counted clockwise from the north.

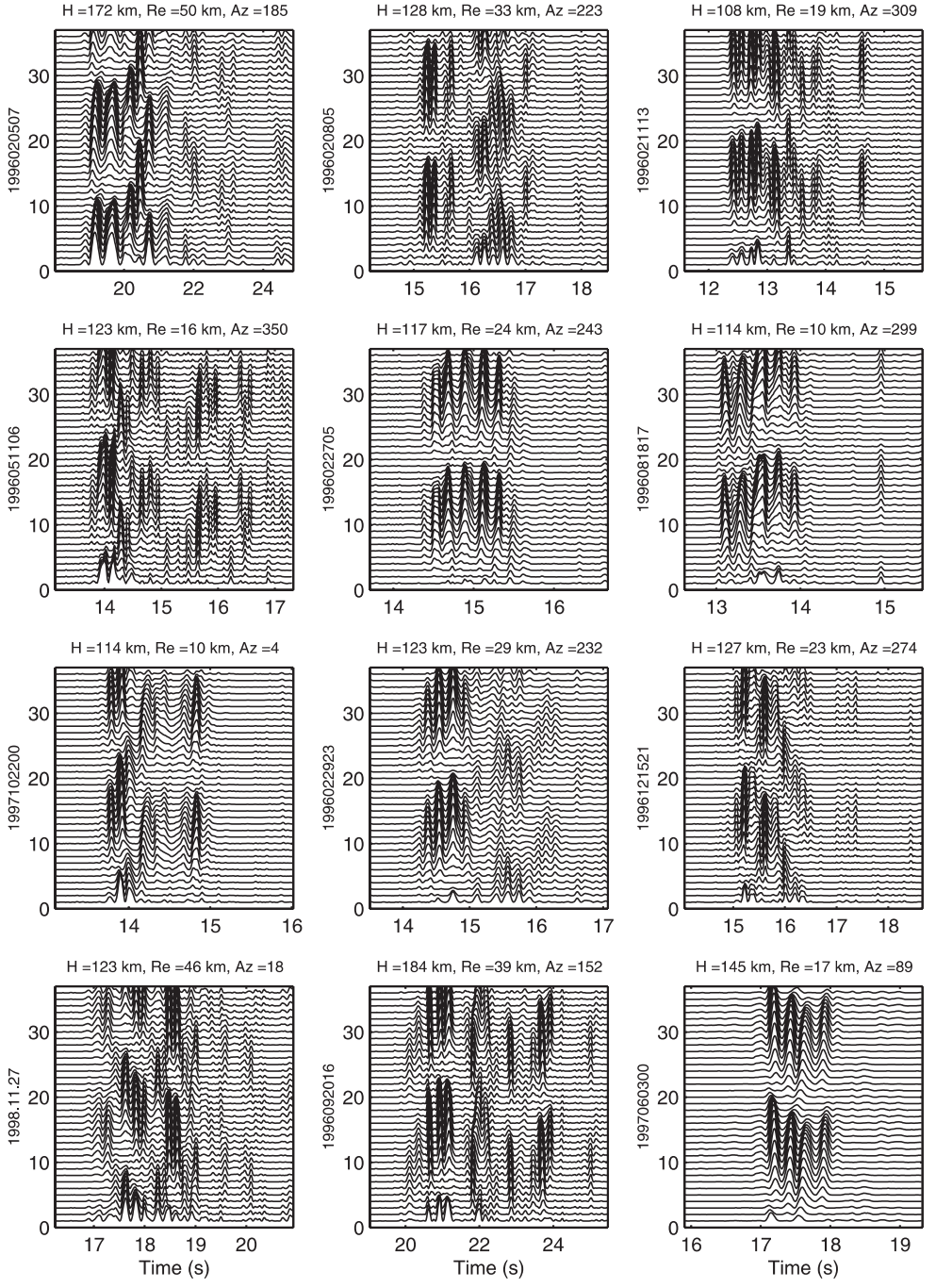

Fig. 11. The same as Fig. 10, but for deep events with the ray path angles less that 17°. The polarization seismograms are grouped into three columns following the event azimuths.

discontinuities. Shear wave patterns for the deep events dated April 20, 1997 (bottom row) give some ambiguity in fast and slow wave recognition. Clearly defined fast and slow waves for the crustal event show a similarity between the waves traced at times after 15.6 s for the deep event.

Fig. 11 demonstrates variations in splitting parameters and shear waves for the deep events with small ray path vertical angles ($\alpha_r < 17°$) and various azimuth directions. For the events of eastern directions, fast azimuths vary from 90° to 140° and time delays change from 0.425 to 1.1 s. The fast azimuths for N–S events vary from 160° to 200°. A significant difference in shear wave fields is observed for the events occurred on February 5, 8, and 11, 1996 (Fig. 11, top row). Fast S-wave azimuths and time delays vary from 20° to 90° and to 140° and from 1.23 to 0.9 and to 0.78 s, respectively. Nevertheless, some similarity can be found among shear wave pattern for the events with different azimuths, for example, between October 22, 1997 (Az = 4°) and December 15, 1996 (Az = 274°), among February 27, 1996 (Az = 243°), August 18, 1996 (Az = 299°) and June 3, 1997 (Az = 89°). Presented polarization seismograms demonstrate instability in shear wave fields and S-wave azimuths for the deep events with comparatively close ray paths located within the 50-km radius around the PET station.

In addition, we have examined the shear wave fields from the quakes with similar hypocenter parameters. Fig. 12 displays polarization seismograms for the deep and crustal events. As could be clearly seen on the polarization seismograms for azimuths around 285° (top row) and 222° (bottom row), the number of the converted waves, their relative amplitudes, and S-wave polarizations differ for the corresponding events. There are certain evidences of simplification of the shear wave field just after large events. Polarization seismograms dated June 15, 1996 (top row) illustrate the simple structure of wave field after the large event of $M \approx 5.2$ (June 13, 1996), whereas seismograms dated January 17, 1998 (bottom row) illustrate complicated wave pattern just 1 day before the earthquake ($M = 5.1$, January 18, 1998). Simple shear wave fields dated May 25, 1998 and May 29, 1998 from crustal events with similar hypocenter parameters are detected just 2 days before and

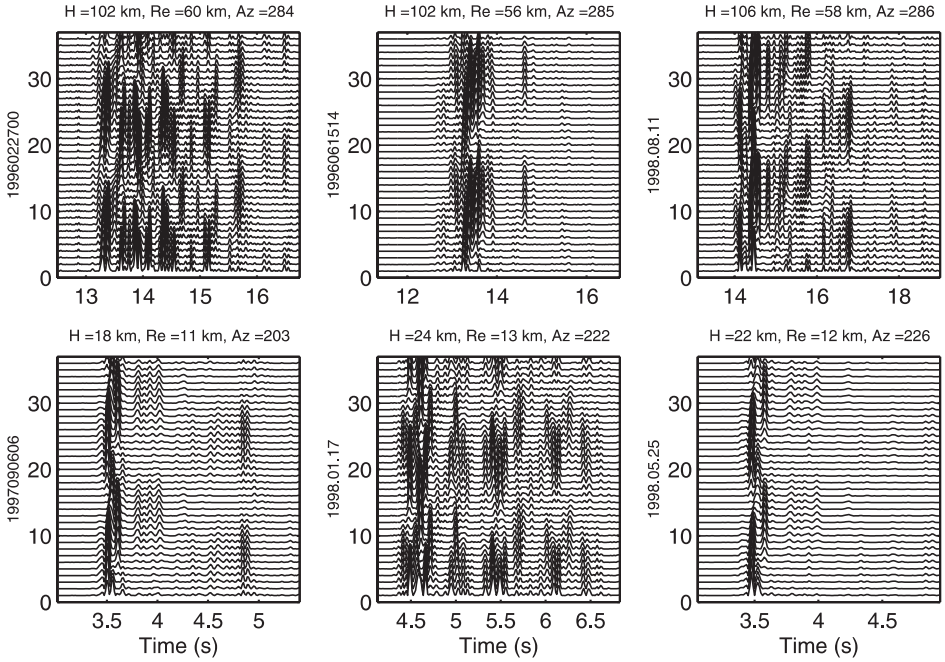

Fig. 12. The same as Fig. 10, but for the events with similar hypocentral parameters.

after the large earthquakes that occurred in the Avacha Bay on May 27, 1998 ($M \approx 5$), May 28, 1998 ($M \approx 6.2$), and June 1, 1998 ($M \approx 6.8$), respectively. A good similarity among the shear wave fields and their splitting parameters is found for the crustal earthquakes dated September 6, 1997, May 25, 1998 (Fig. 12), May 29, 1998 ($H = 17$ km, $R_e = 11$ km, Az = 230°), and July 1, 1998 ($H = 21$ km, $R_e = 11$ km, Az = 227°).

4.4. Temporal variations in shear wave splitting

Figs. 13 and 14 demonstrate temporal variation in normalized time delays in two bands for the crustal, upper mantle events ($H < 80$ km), and deeper events, respectively. A nearest neighbor interpolation of data with 1-day step and later averaging with a three-point moving window were applied. Solid line represents interpolated and averaged data. To estimate a

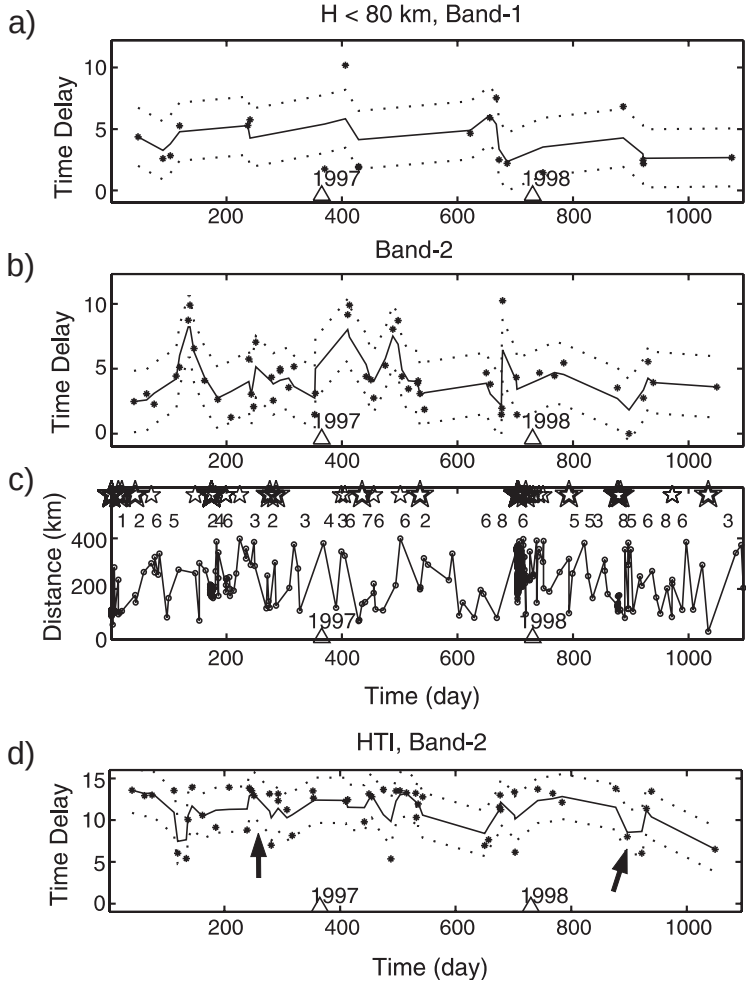

Fig. 13. (a and b) Temporal variation in normalized time delays over 1996–1998 for the crustal and upper mantle events ($H < 80$ km) in two bands at ±15° (Band 1) and 15–45° (Band 2) to the crack strike, respectively. The solid lines are three-point moving average. Dotted lines indicate 68% confidence interval. (c) Epicentral distances of large earthquakes ($M > 4$) occurred at distances less than 400 km from PET over the 3-year period. Stars mark the origin time of large events ($M \geq 5$). The large stars mark the events that occurred at distances less than 200 km. The numbers below the stars specify the area of earthquake locations shown in Fig. 1b. (d) Normalized time delays calculated for the HTI model and distributed with time in accordance to the location and origin time of the events for the observed data in Band 2. The solid line is a three-point moving average. Dotted lines indicate 68% confidence interval.

possible correlation between changes in shear wave parameters and seismic activity, temporal distribution of large events ($M \geq 5$) and epicentral distances of large events ($M \geq 4$) relative to the PET are presented in Figs. 13c and 14c.

As could be seen in Fig. 13b, the greatest values of δt_{SS} up to 10 ms/km are detected at 120–130-day interval between the large earthquakes in the north area (Karymsky earthquake, $M=7$, zone 1) and the earthquakes series in the Avacha Bay (June 21–23, 1996, $M=5.3–7.1$, zone 2, Fig. 1b), and at 670–680-day interval before the Kronotsky Earthquake ($M=7.7$). Time delay increases are observed also near the 410th and 490th days may be associated with the largest events in south area of the Avacha Bay. During 1998 year, δt_{SS} behave almost stable varying around 3–5 ms/km. Time delays in Band 1 changed slightly in 1996–1997 and decreased in 1998 (Fig. 13a). The number of data in Band 1 is too small to generalize δt_{SS} variations with time. At the same time, δt_{SS} did not display any substantial disagreement with the data in Band 2. In order to estimate possible δt_{SS} variations caused by events locations in Band 2, time delays are calculated for the HTI model in accordance with the location and origin time of the events for the observed data (Fig. 13d). The calculated data are distributed almost uniformly with increased scattering in some short intervals and hardly correlate with the observed data. Neverthe-

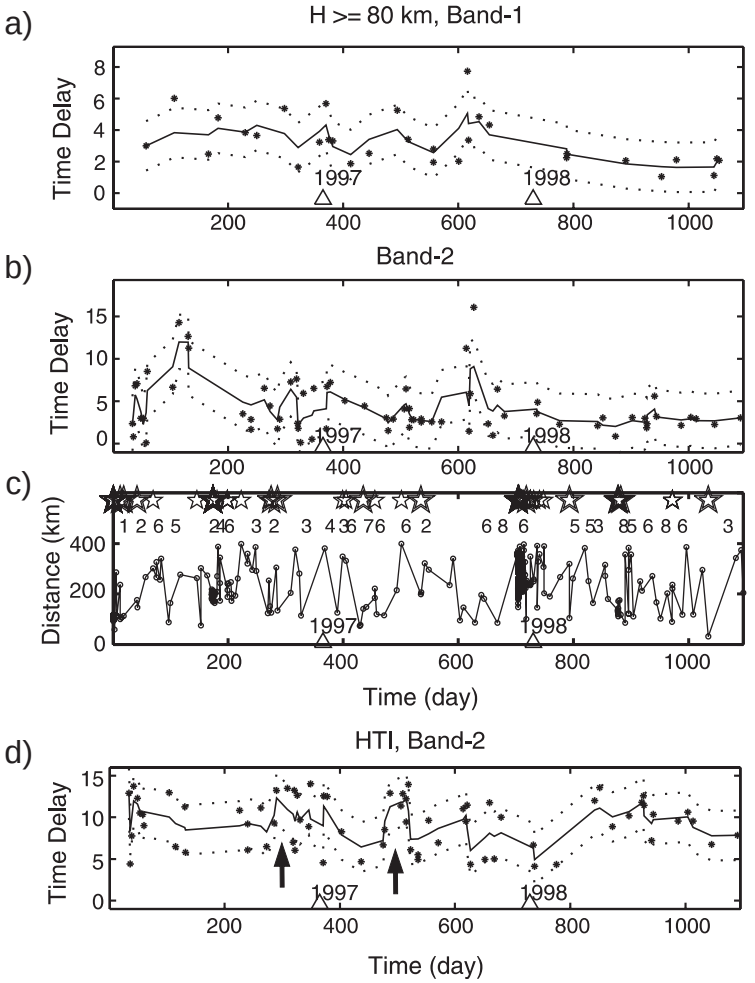

Fig. 14. The same as Fig. 13, but for deep events ($H \geq 80$ km).

less, calculated δt_{SS} increase and decrease near 240–250 days and 900th day (marked by arrows in Fig. 13d) correlate well with the observed changes. Thus, these changes in the observed data should be omitted. At the same, since the observed greatest values of δt_{SS} correspond to the decreased or stable values of calculated δt_{SS}, they may be considered as significant and independent from the event location.

Time delays for the deep events reveals similar tendency in variations (Fig. 14). The greatest values (up to 7.7 ms/km) are detected near the 620th day, 85 days before the Kronotsky Earthquake in Band 1. In the Band 2, two clear time delay increases are observed at the day intervals of about 100–130 and 610–670. During 1998, δt_{SS} are stabilized at the level of 2–3 ms/km. Figs. 14d and 15 represent scattering of δt_{SS} calculated for the HTI model in Band 2 and for the orthorhombic model in the two bands, respectively. The distribution of δt_{SS} with time for the HTI reveal more complicated scattering and in a larger range of values, while those for the orthorhombic model are scattered more compactly and without significant fluctuations. In time intervals of about 260–370 and 480–520 days (marked by arrows in Fig. 14d), δt_{SS} reveal a similarity with the calculated data for HTI model and may be considered as location effects. As a whole, if we exclude the huge increases of δt_{SS} before the Avacha earthquakes and Kronotsky Earthquake, δt_{SS} changes smoothly with time and shows a better agreement with the calculated δt_{SS} presented in Fig. 15. Unfortunately, the data are distributed very unevenly in time, and behavior of time delays near the origin time of large earthquakes remains to be unclear. For both groups, the increased time delays are observed between very large events.

The fast shear wave polarizations manifest more complicated changes with time. Fig. 16a and b represent $\varphi(t)$ variations for the events of Group 1 ($H < 80$ km) and Group 2 ($H \geq 80$ km) in band at $\pm 45°$ (Band 3) to the crack plane within effective shear wave window. Anomalous changes in φ are observed in the periods of about 40–120, 220–250, 370–385, and 920–930 days and before the Kronotsky Earthquake in 500–680-day interval. Temporal sequences $\varphi(t)$ disclose the general tendency to the cyclic changes. Visually, three cycles in $\varphi(t)$ could be clearly distinguished until about 500th day for the data of both groups. Fast azimuths of the two groups reveal almost synchronous variation during 500 days. The

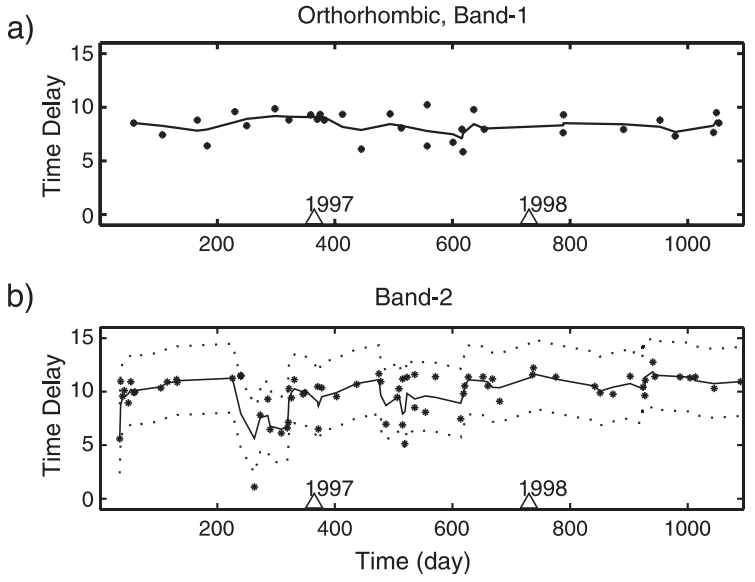

Fig. 15. Normalized time delays calculated for the orthorhombic model and distributed with time in accordance to the location and origin time of the events for the observed data in the two bands. The solid line is a three-point moving average. Dotted lines indicate 68% confidence interval.

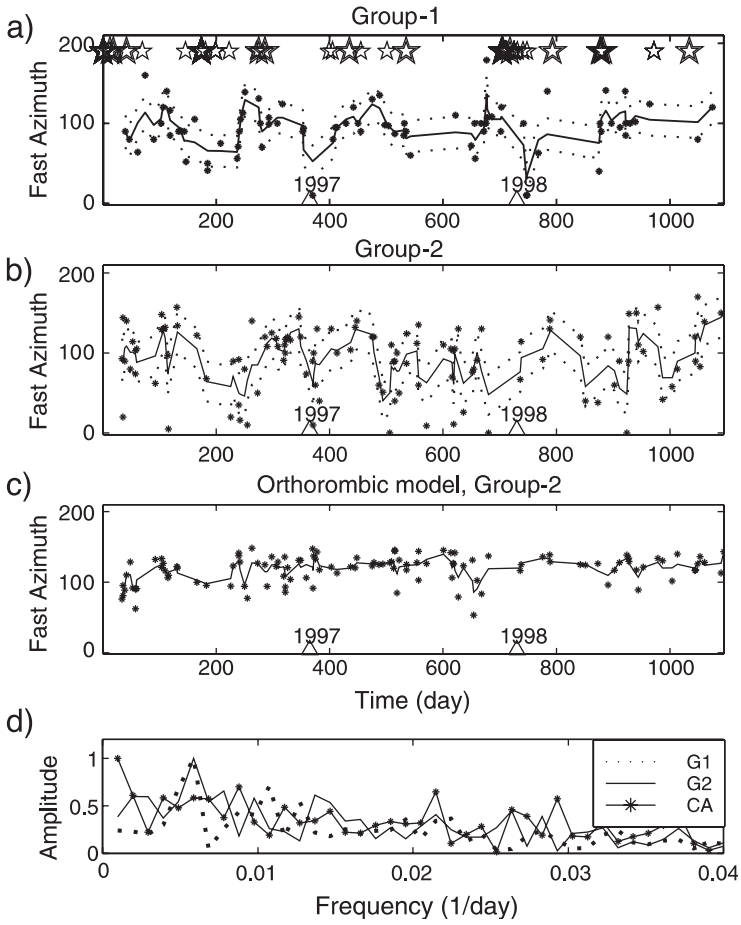

Fig. 16. (a and b) Temporal variation in the fast S-wave polarization azimuths over 3 years for events with depths at upper 80 km (Group 1) and lower 80 km (Group 2) in the band at $\pm 45°$ (Band 3) to the crack strike. The solid lines are three-point moving average. Dotted lines indicate 68% confidence interval. Stars mark the origin time of large events ($M \geq 5$). The large stars mark the events that occurred at distances less than 200 km. (c) Fast S-wave polarization azimuths calculated for the orthorhombic model and distributed with time in accordance to the location and origin time of deep events for the observed azimuths in Band 3. The solid line is a three-point moving average. (d) Fourier spectra normalized by the maximum amplitude of observed fast polarization azimuths in two groups (G1, G2) and those calculated for the orthorhombic model (CA).

data of crustal events ($H \leq 35$ km), whose number is too low and amounts to 17% (23 points) in Group 1, behave more stable with time giving average value and standard deviation of about 96° and 19°, respectively. The observed changes in $\varphi(t)$ (Fig. 16b) are mainly formed by the data of upper mantle events.

Possible variation in $\varphi(t)$ caused by the event locations were estimated for the orthorhombic model for the deep events in Band 3 and shown in Fig. 16c. The calculated fast azimuths $\varphi(t)$ are scattered with time in a smaller range around 100° comparing with the observed data. Fig. 16d demonstrates Fourier spectra normalized by the maximum amplitude for the temporal sequences of $\varphi(t)$ in the two groups and for calculated data $\varphi_0(t)$. Since the data are distributed unevenly with time, the observed sequences of $\varphi(t)$ were interpolated between nearest neighbors with 1-day step after an averaging of φ for the events occurred just at 1 day. A spectral amplitude maximum with the periods of about 172 days is found in $\varphi_0(t)$ for both the groups, while $\varphi_0(t)$ does not reveal any dominant period.

Temporal variation in calculated fast azimuths was examined for different realistic sampling in accordance to the event locations of the observed data. In fact, calculated sequences may show a harmonic-like variation with the distinct dominant spectral periods which, however, change from one sampling to another. Small changes in data set bring significant spectrum changes. This spectrum instability reveals that any detected Fourier peak is insignificant and accidental. Unlike this, the period of about 172 days reveal stability for different samplings of the observed data. Therefore, we think that the periodical temporal variation in observed fast azimuths is statistically significant and does not significantly depend on the event locations. The variation in fast S-wave azimuths allows to be approximated by a simple harmonic function $y(t)=\varphi_0+A\cos(2\pi\varphi(t)/T+\vartheta)$ with the period $T\approx 172-175$ days, amplitude $A=30-40°$, and reference level $\varphi_0=90°$. The distribution of deviations $D_y\varphi(t)=y(t)-\varphi(t)$ for various sampling satisfies well to the normal distribution at the 68% and 95% confidence intervals.

5. Discussion and conclusions

5.1. Anisotropy of medium

For the 3-year period of 1996–1998, the dominant fast S-wave azimuths are aligned to 80–110°, which are consistent with the direction of the Pacific Plate motion at the South Kamchatka in general. The fault plane solutions for the main shock of the Kronotsky Earthquake and the large aftershocks give similar azimuths of the compressive stress in the range from 97° to 129° following Harvard CMT (Gusev et al., 1998). In the period of 1990–1993, the fast S-wave polarizations were determined along $70\pm10°$ for the PET area (Chesnokov et al., 1992; Krasnova and Chesnokov, 1998). Based on the GPS study in Kamchatka during 1996–1997 (Takahashi et al., 1999), the motion direction of the PET site with respect to the Eurasian plate was estimated about 330°. The last data show some diversity in the dominant motion at the PET area.

The anisotropy coefficients increase with depth from 1–2% in the crust to 4% in the upper mantle. The largest value of the anisotropy coefficient up to 7.5% is observed for the event that occurred in the subducting slab at the depth interval of 90–140 km. However, due to a broad scattering in time delays, the average anisotropy coefficients give low values about 1%, 1.6%, and 1.8% for the crust, upper mantle, and subducting slab, respectively. The increased time delay scattering is detected in the NE and SSE directions during 1996–1997.

Modeling of fast shear wave polarizations shows that HTI model with the symmetry axis oriented to $15\pm10°$ fits well the observed data. Fast S-wave polarizations agree particularly well with those predicted for the events located in the upper 80-km depth and in the east directions. The 16% of fast S-wave azimuths deviate anomalously from the predicted azimuths. The anomalous azimuths are mainly associated with the deep events (H>80 km) and event back-azimuths along N–NE and SSW directions. The uncertainty in φ is also observed for the deep events with close locations and ray path inclinations less than 20°. The proposed alternative orthorhombic model does not show significantly better or worse fitting results for the observed polarizations and time delays of deep events. At the same time, comparison between the deep event fast azimuths of the direct shear waves and small-amplitude split waves traced ahead of the direct shear wave arrival time, which are considered as converted waves at upper medium discontinuities, shows either good agreements or disagreements. This suggests that variations in φ may have a temporal character and may be caused either by reactivation of pre-existing faults (fracture zones) of corresponding directions or by the local stress changes, or by both. Analysis of fault plane solutions of crustal earthquakes (Harvard CMT Catalogue) shows that reversed faults prevail during 1996–1998 in the Kamchatka region, although normal faults have livened up in some periods. Active normal fault developing was detected from the end of 1995 and to February 1996 resulting in the Karymsky Earthquake and the Karymsky Volcano eruption in the northern area from PET. In that period, the anomalous values of φ, especially from the north and south events, might be aligned to the extension axis. The observed anomalous values of φ and δt_{SS} for events around NNE and SSE back-azimuths in 1996–1997 might be considered as pre-event effects developing along

the faults/fracture zone parallel to the strikes of nodal planes of the Kronotsky Earthquake.

5.2. Temporal variations in shear wave splitting

Examination of temporal variations in splitting parameters for different data samplings allows us to make some conclusions. Variation of time delays in the two bands shows generally increased values in 1996–1997 and comparatively stable behavior at level of 2–4 ms/km in 1998. The most rapid and distinct changes in δt_{SS} correlate with very large crustal events that occurred in the Avacha Bay at the distances less than 200 km from PET. The greatest time delays are detected up to 10 ms/km for the crustal and upper mantle events and up to 16 ms/km for the deep events before the earthquake series in the Avacha Bay (June 21–23, 1996; $M=5.3–7.1$, zone 2, Fig. 1b), and the Kronotsky Earthquake (December 5, 1997; $M=7.7$). Before the Kronotsky Earthquake (705th day), δt_{SS} increased around the 620th day for the deep events and 670th day for the crustal and upper mantle events. Before the earthquake series in the Avacha Bay (173rd day), δt_{SS} increase is detected in the 100–130-day interval for the deep events and the 120–130-day interval for the crustal and upper mantle events. Unfortunately, the data are distributed unevenly with time and not very dense, and behavior of δt_{SS} near the origin time of very large earthquakes remains to be unclear. As a rule, the increased time delays are observed between very large events.

The temporal variation in fast S-wave azimuths reveals complicated behavior during the study period. The most sharp changes in φ tend to occur around the origin time of the largest earthquakes. Anomalous fast azimuths are observed at about the 500–680-day interval before the Kronotsky Earthquake and after that during the 730–740-day interval. A difference in the intensity and behavior among variations of $\varphi(t)$ for the crustal, upper mantle, and deep events are detected. The fast azimuths of crustal events show the most stable behavior, although their number is too small for sure judgment. On average, temporal variation in $\varphi(t)$ of deep events manifests harmonic-like oscillations in broad azimuth range with dominant period of about 172 days over a 3-year period. The variation in $\varphi(t)$ of upper mantle events reveals similar periodical oscillations of smaller order in 1996–1997 and tends to stabilize in 1998. The harmonic functions with the periods of about 172–175 days and amplitude of 30–40° fit well the data from the crustal and mantle events. Deviations ($D_{y\varphi}(t)=y(t)-\varphi(t)$) for all data and various samplings satisfy well to the normal distribution at the 68% and 95% confidence intervals.

If we consider that the study medium pertains to the HTI symmetry and orientation of the symmetry elements is stable with time, then observed variation in fast S-wave azimuths can be explain by either measurement errors or medium heterogeneities. Since a number of records reveal an ambiguity in the fast and slow shear wave recognitions, different variants of the measurement were used to minimize the errors. We have applied different measurement variants to the data, but they do not alter the final results significantly. Another source of discrepancy between theoretical and observed data may associate really with the application of homogeneous models of medium. Unfortunately, the model improving requires our knowledge about S-wave velocity structure and anisotropic properties of the layers, which are weakly known for the study area now. At the same time, the data analysis shows that there is no significant statistical evidence about the fast S-wave azimuth dependence on the event back-azimuth and ray path inclination.

If we consider that the study medium differs from the HTI model, then data variations may be caused by event locations. We have examined variations of split shear wave parameters with time for the orthorhombic model for a variety of sampling in accordance to the event locations of the observed data. In contrast to the observed data, calculated sequences are scattered quite more uniformly with time in the limited range of values and, in general, hardly correlate with the observed data. In fact, calculated sequences may reveal harmonic-like variations with the distinct dominant spectral period which, however, changes from one sampling to another. Small changes in calculated data set bring significant spectrum changes. This spectrum instability reveals that any detected Fourier peak is insignificant and accidental. Unlike this, the period of around 172 days in the observed fast azimuth temporal variation is detected for different samplings. Therefore, we think that the periodical temporal variation in observed fast azimuths may be considered as independent of event locations and statistically significant. On the other hand, the data

are scattered unevenly with time, and spectral analysis was applied to the interpolated data which reflect mainly the tendency. Therefore, we do not insist on the periodical variation in $\varphi(t)$, but we cannot also say that fast azimuths of mantle events are distributed uniformly with time.

Analysis of the shear wave field and number of converted waves (or relative intensity of converted waves) for various close event locations also shows their temporal changes. On the other hand, a good similarity between shear wave fields and polarizations of split shear waves from the events of different locations registered on the same day was observed. This indicates that the mechanical state of the medium or apparent layering of the medium may change. The apparent lamination (layering) of the medium may be significantly intensified in the period of large earthquake preparation and turn into the almost homogeneous state just before or after the earthquake.

The temporal variation observed in the fast S-wave polarizations appear to be the unusual result and raise many questions. Although there is an agreement between splitting parameter changes and time of some large earthquake occurrences in the region, we do not think that the shear wave splitting changes can be explained only as pre- and post-event effects. The existence of additional stress-related process acting during the observation period is assumed. The data manifest clearly the difference in character and intensity of splitting parameter variations observed in the first 2 years and in the last year, although the regional seismicity level has not been appreciably changed. Since the more intensive variations in the fast S-wave polarizations are observed for the events with depths greater than 80 km, it suggests that the major stress instabilities are localized in the subducting slab. Presently, it is difficult to judge definitely what the source may cause the regular variations in shear wave parameters with the period of 172 days, which is close to the seasonal cycle. At the same time, it is interesting that the origin times of very strong earthquakes ($M \geq 7.7$) that occurred in the Kronotsky Bay and Kamchatsky Bay during the last century have a propensity to the winter time: December 15, 1971 ($M = 7.8$; 55.9°N, 163.4°E), February 3, 1923 ($M = 8.5$; 53°N, 161°E), January 30, 1917 ($M = 8.1$; 55.2°N, 164.5°E).

The preliminary results of GPS study during 1997–2000 on the Kamchatka Peninsula show that a vast area was involved in the deformation process during the Kronotsky Earthquake (Gordeev et al., 2001). Significant pre- and post-seismic GPS variations were detected. Half a month before the Kronotsky Earthquake, precursory deformation signals were clearly detected at stations KLU, ES1, and KBG. Since stations KLU, KBG, and ES1 were operated from 1996, it became possible to compare velocity motions defined with respect to the station PETP before and after the Kronotsky Earthquake (Gordeev et al., 2001). The total angular differences in the motion directions of KLU, KBG, and ES1 sites amount to about 26°, 158°, and 152°, respectively.

Analysis of geodynamics of Eastern Kamchatka shows that Petropavlovsky and Shipunsky blocks, located near the plate edge, participate periodically in two motions of about trench-normal and trench-parallel directions due to the oblique subduction and mantle flow uplifting beneath the East Kamchatka Volcanic Belt (e.g., Legler, 1978). The estimated block motion velocities are much smaller than the motion velocity of the subducting Pacific Plate. According to the hydrodynamic study at the 665-m-deep Elizovskaya-1 observation well located at 30 km from Petropavlovsk–Kamchatski and operated since 1987 (Kopylova, 1999, 2001), the general long-term water level decrease was observed since 1990–1991 from the maximum groundwater level of about −27.5 m. On May 20, 1997 (200 days before the Kronotsky Earthquake) the water level has reached the minimum value at the 29.15-m depth and started to increase gradually. During 1996–1997, two significant post-seismic water level rises of about 0.15 and 0.3 m were recorded just after the Karymsky and Kronotsky Earthquakes, respectively. After the Kronotsky Earthquake, water level continues to rise. The change in sign of the long-term groundwater level gradient in 1989–1990 and 1997 suggests the corresponding change in dynamic regime in the medium under study. Based on the geodesic measurements at the Petropavlovsk polygon, it was found the transition in rock strain from the compression to extension stage in the period of 1988–1990 (Kopylova, 1999). Following these, we may assume that the ratio of principal stress components might be not very stable during the study period, and this situation might bring to the corresponding fluctu-

ations in physical parameters and symmetry axis orientation of the medium. Stress variations may be caused by different secondary sources: (a) irregular process of plate subduction along the arc; (b) temporal variation in motion rate of subducting plate; and (c) temporal variation in mantle flow uplift, etc. A medium ordering or self-organizing embraces a large range of dimensions from cracks and grains to the fractures and blocks.

Acknowledgements

The authors are grateful to A. Viculin, D. Droznin, and V. Levina for their help in work with earthquake records and catalogue and to Kamchatka Experimental Methodical Seismological Department of GS RAS for providing the seismic records used. This work was supported by the Russian Foundation for Basic Research (Grant 99-05-64863) and Korean Research Foundation Grant (KRF-2000-015-DP0431). We are grateful to the editor and anonymous reviewers for their constructive comments.

References

Aizenberg, A.M., Klem-Musatov, K.D., Landa, E.I., 1974. Model of anisotropic seismic media. Seismic Waves in Complex Media. Nauka, Siberia Branch AN SSSR, Novosibirsk, pp. 64–109 (in Russian).

Bokelman, G.H.R., Harjes, H.P., 2000. Evidence for temporal variation of seismic velocity within the upper continental crust. J. Geophys. Res. 105 (B10), 23879–23894.

Chesnokov, E.M., Krasnova, M.A., Abaseev, S.S., Tarasov, N.T., Maximov, A.B., Gavrilov, V.F., Gordeev, E.I., 1992. Shear wave polarization study from local earthquakes of small energy. Seismic Wave Fields. Nauka, Moscow, pp. 34–48 (in Russian).

Crampin, S., 1990. Seismic fracture anisotropy in the Earth's Crust: an overview. J. Geophys. Res. 95 (B7), 11105–11114.

Crampin, S., 1991. Wave propagation through fluid-filled inclusions of various shapes: interpretation of extensive-dilatancy anisotropy. Geophys. J. Int. 104, 611–623.

Crampin, S., 1998. Stress forecasting: a viable alternative to earthquake prediction in a dynamic Earth. Trans. R. Soc. Edinb.: Earth Sci. 89, 121–133.

Crampin, S., 1999. A successfully stress-forecast earthquake. Geophys. J. Int. 138, F1–F5.

Crampin, S., Booth, D.C., 1989. Shear-wave splitting showing hydraulic dilatation of pre-existing joints in granite. Sci. Drill. 1, 21–26.

Crampin, S., Lovell, J.H., 1991. Decade of shear wave splitting in the Earth's crust: what does it mean? What use can we make of it? And what we should do next? Geophys. J. Int. 107, 387–407.

Dyadkov, P.G., Melnikova, V.I., Sankov, V.A., Nazarov, L.A., Nazarova, L.A., Timofeev, V.Yu., 2000. Recent geodynamics of the Baikal rift: stages of compression and further extension during 1992–1996. Proc. Acad. Sci. (DAN) 372 (1), 99–103 (in Russian).

Galperin, E.I., 1984. The polarization method in seismic exploration. Dordrecht, Boston Reidel Pub., Hingham, MA, USA. 268 pp.

Gledhill, K.R., Stuart, G., 1996. Seismic anisotropy in the fore-arc region of the Hikurangi subduction zone, New Zealand. Phys. Earth Planet. Inter. 95, 211–225.

Gorbatov, A., Dominguez, J., Suarez, G., Zhao, D., Gordeev, E., 1999. Tomographic imaging of the P-wave velocity structure beneath the Kamchatka peninsula. Geophys. J. Int. 137, 269–279.

Gordeev, E.I., Gusev, A.A., Levin, V.E., Bahtiyarov, V.F., Pavlov, V.M., Chebrov, V.N., Kasahara, M., 2001. Preliminary analysis of deformation at the Eurasia–Pacific–North America plate junction from GPS data. Geophys. J. Int. 147, 189–198.

Gusev, A.A., Pavlov, V.M., 1998. Preliminary determination of parameters of high-frequency radiator in the source of Kronotsky Earthquake (Dec. 5, 1997, Mw = 7.9, Kamchatka). Kronotsky Earthquake of December 5, 1997, on Kamchatka: Precursors, Properties, Effects. Kamchatka State Academy of Fishing Marine, Petropavlovsk–Kamchatski, pp. 68–79 (in Russian).

Gusev, A.A., Levina, V.A., Saltykov, V.A., Gordeev, E.I., 1998. Large Kronotsky Earthquake on Dec.5, 1997: basic data, seismicity of epicentral zone, source mechanism, macroseismic effects. Kronotsky Earthquake of December 5, 1997, on Kamchatka: Precursors, Properties, Effects. Kamchatka State Academy of Fishing Marine, Petropavlovsk–Kamchatski, pp. 32–54 (in Russian).

Hsu, C.J., Schoenberg, M., 1993. Elastic waves through a simulated fractured medium. Geophysics 58 (7), 964–977.

Hudson, J.A., 1981. Wave speeds and attenuation of elastic waves in material containing cracks. Geophys. J. R. Astron. Soc. 64, 133–150.

Ilchenko, V.L., Gorbatsevich, F.F., 1999. Changes in space position of symmetry elements in anisotropic rock under applied stress. Phys. Earth 5, 40–46 (in Russian).

Kaneshima, S., 1990. Origin of crustal anisotropy: shear wave splitting studies in Japan. J. Geophys. Res. 95 (B7), 11121–11133.

Kaneshima, S.M., Ando, M., Crampin, S., 1987. Shear wave splitting above small earthquakes in the Kinki district of Japan. Phys. Earth Planet. Inter. 45, 45–58.

Kopylova, G.N., 1999. Relation between seismicity and ground water level variation in deep well (Elizovskaya-1 well), Kamchatka, 1987–1998. Structure and Evolution of the East Asia. Institute of Tectonics and Geophysics FB RAS, Khabarovsk, pp. 303–313 (in Russian).

Kopylova, G.N., 2001. Variations of water level in Elizovskaya-1 well, Kamchatka due to large earthquakes: 1987–1998 observations. Volcanol. Seismol. 2, 39–52 (in Russian).

Krasnova, M.A., Chesnokov, E.M., 1998. On shear wave polariza-

tion changes in the crust of Kamchatka based on records of local earthquakes. Volcanol. Seismol. 4–5, 138–148 (in Russian).

Kuzin, I.P., 1974. Focal Zone and the Upper Mantle Structure in the Region of Eastern Kamchatka Nauka, Moscow. 131 pp. (in Russian).

Legler, V.A., 1978. Recent faults and horizontal tectonic motions in the Eastern Kamchatka. PhD thesis, Russian Academy of Sciences Khabarovsk. 158 pp. (in Russian).

Liu, Y., Crampin, S., Main, I., 1997. Shear wave anisotropy: spatial ant temporal variation in time delay at Parkfield, Central California. Geophys. J. Int. 130, 771–785.

Liu, E., Hudson, J.A., Pointer, T., 2000. Equivalent medium representation of fractured rock. J. Geophys. Res. 105 (B2), 2981–3000.

Luneva, M., Young, Y.F., 1995. Scattering of elastic waves by a thin soft layer. J. Seism. Explor. 4, 17–32.

Schoenberg, M., 1980. Elastic wave behavior across linear slip interfaces. J. Acoust. Soc. Am. 68, 1516–1521.

Shin, X.R., Meyer, R.P., Schneider, J.F., 1989. An automated, analytical method to determine shear wave splitting. Tectonophysics 165, 271–278.

Silver, P.G., Chan, W.W., 1991. Shear wave splitting and subcontinent mantle deformation. J. Geophys. Res. 96 (B16), 16429–16454.

Sobolev, G.A., 1999. Stages of Kamchatka strong earthquake preparation. Volcanol. Seismol. 4–5, 63–72 (in Russian).

Sobolev, G., 2001. The examples earthquake preparation in Kamchatka and Japan. Tectonophysics 338, 269–279.

Takahashi, H., Kasahara, M., Kimata, F., Miura, S., Heki, K., Seno, T., Kato, T., Vasilenko, N., Ivashenko, A., Bahtiyarov, V., Levin, V., Gordeev, E., Korchagin, F., Gerasimenko, M., 1999. Velocity field of around the Sea of Okhotsk and Sea of Japan regions determined from a new continuous GPS network data. Geophys. Res. Lett. 26 (16), 2533–2536.

Wolfe, C.J., Silver, P.G., 1998. Seismic anisotropy of oceanic upper mantle: shear wave splitting methodologies and observations. J. Geophys. Res. 103, 749–771.

Yanovskaya, T.B., Dmitrieva, L.A., 1991. Influence of non-rigid contact of elastic media on transmission, reflection and conversion coefficients. Phys. Earth 2, 45–52 (in Russian).

Zatsepin, S., Crampin, S., 1997. Modeling the compliance of crustal rocks: I. Response of shear wave splitting to differential stress. Geophys. J. Int. 129, 477–494.